Available online at www.sciencedirect.com
SCIENCE DIRECT®
International Journal of Solids and Structures 42 (2005) 2533–2558
INTERNATIONAL JOURNAL OF SOLIDS and STRUCTURES
www.elsevier.com/locate/ijsolstr

Phase field dependent viscoplastic behaviour of solder alloys

R.L.J.M. Ubachs *, P.J.G. Schreurs *, M.G.D. Geers

Department of Mechanical Engineering, Section of Materials Technology, Eindhoven University of Technology, P.O. Box 513, 5600 MB Eindhoven, The Netherlands

Received 14 July 2004; received in revised form 6 October 2004
Available online 23 November 2004

Abstract

A phase field model is presented to describe the mechanical behaviour of microstructure dependent materials, which is demonstrated by applying it to eutectic tin–lead solder. This solder material is known to be heavily influenced by its continuously evolving microstructure. For the constitutive behaviour of the different phases the elasto-viscoplastic Perzyna model has been used. It is coupled to the phase field model through the constitutive parameters which are taken dependent on the mass fraction field resulting from the solution of the phase field equations.

Keywords: Viscoplasticity; Phase field model; Tin–lead solder; Microstructure dependence

1. Introduction

Solder joints serve two important purposes. Firstly, they form the electrical connection between the component, e.g. a chip or resistor, and a substrate, e.g. a printed circuit board. Secondly, they constitute the mechanical bond that holds the component fixed to the substrate. During their life the joints are subjected to combined thermal and mechanical stresses which considerably impacts the fatigue lifetime. Therefore, their resistance to fatigue under thermal cycling is an important mechanical property of solder joints. Because of time limitations solder joints are often tested for their thermo-mechanical fatigue properties by subjecting them to accelerated test methods. However, during these accelerated experiments, damage mechanisms might be exhibited by the solder alloy which do not occur during normal usage. Reversely, some failure mechanisms are governed by time constants which are not reached in these test methods. Predictions

* Corresponding authors. Tel.: +31 40 247 4022; fax: +31 40 244 7355 (R.L.J.M. Ubachs), tel.: +31 40 247 2778; fax: +31 40 244 7355 (P.J.G. Schreurs).
E-mail addresses: r.l.j.m.ubachs@tue.nl (R.L.J.M. Ubachs), p.j.g.schreurs@tue.nl (P.J.G. Schreurs).

0020-7683/$ - see front matter
doi:10.1016/j.ijsolstr.2004.10.008

based on accelerated cycling tests are therefore unreliable. Thermo-mechanical modelling could help to simulate the real life conditions of a solder joint and thus give a more accurate prediction of its lifetime. Furthermore these techniques permit a significant reduction in cost and time of the design of highly reliable soldered connections in electronic packaging and surface mount technology.

The service temperature T of solder alloys is typically above half of their melting temperature T_m, i.e. their homologous temperature T_H, which is the ratio between T and T_m is greater than 0.5. Because of this the deformation behaviour is governed by high temperature mechanisms like creep, grain boundary sliding, and relaxation. Therefore, in literature when modelling the mechanical behaviour of solder alloys, use is generally made of viscoplastic material models (Amagai, 1999; Basaran and Chanderoy, 2000). Numerous creep rate functions have been proposed, for which an extensive review can be found in Ju et al. (1994). One of the commonly used viscoplastic models for solder alloys is the Anand model (Anand, 1985). This model does not have an explicit yield condition, and thus there will be no discrete switching between elastic and viscoplastic behaviour. This should improve the numerical efficiency of the model. Furthermore, the model contains a single internal variable that represents the resistance against inelastic flow. A drawback of this model is that it contains many nonstandard parameters which need to be determined. In this contribution the viscoplastic strain rate function defined by Perzyna (1966) is used to describe the time dependent mechanical behaviour (Sluis et al., 1999). In literature it is most commonly used to model secondary creep: (Basaran et al., 1998; Ju et al., 1994). Its parameters are more transparent than those of the Anand model and adaptation of the hardening law is straightforward, leading to a highly flexible model. The standard Perzyna's strain rate function does not account for grain size and temperature dependent creep activation energy and power law break down region of creep. It is well known that grain/phase size makes a significant difference in solder alloy behaviour, and that the overall joint properties are heavily affected by the microstructure (Basaran and Chanderoy, 1998; Basaran and Tang, 2002). Vice versa, the evolution of the microstructure is affected by the stress state in the material. The Sn–Pb system is known to coarsen under the influence of thermal or thermomechanical loading (Hacke et al., 1998; Matin et al., 2004; Vianco et al., 1999). Frear et al. (1988) found that regions of high shear strain within an eutectic tin–lead connection coarsened more. These regions of inhomogeneous coarsening are known to be crack nucleation sites during thermal cycling (Frear, 1989; Hacke et al., 1998).

Various attempts have been made to include a microstructural variable like the average grain or phase size in the mechanical model for a solder material (Basaran and Chanderoy, 1998, 2000; Frear et al., 1997; Vianco et al., 1999). In the literature several equations can be found to describe grain size coarsening (Clark and Aldan, 1973; Lifshitz and Slyozov, 1961; Senkov and Myshlyaev, 1986), however no information about the distribution or shape of the grains is given. More information about the microstructure can be obtained by using a diffuse interface model (Cahn and Hilliard, 1958). These models are based on the notion that the free energy is not only a function of a local order parameter, but also depends on the value of this parameter in its immediate neighbourhood. In this way the contribution of an interface to the free energy is included. Minimisation of the free energy then leads to coarsening of the system through the reduction of interfaces, either grain or phase boundaries (Dreyer and Müller, 2000; Leo et al., 1998; Ni et al., 2002; Ubachs et al., 2004; Zhu et al., 1999).

In various papers the influence of infinitesimal elastic strains on the evolution of the microstructure is investigated (Artemev et al., 2000; Dreyer and Müller, 2001; Ni et al., 2002; Zhu et al., 2001). In this paper, however, a phase field model is coupled to a finite strain elasto-viscoplastic model to investigate the impact of the underlying microstructure. First, the evolution of the microstructure is dealt with using a phase field model based on a strongly nonlocal mass fraction which accounts for the evolution under thermal loading (Ubachs et al., 2004). The phase field provides extensive information on the microstructure: the mass fractions of the individual phases, their shape and orientation, and position and shape of interfaces between phases. This information is further used to determine local material parameters for the constitutive material model applied, i.e. a viscoplastic Perzyna model. In this way a microstructure dependent mechanical model for multiphase alloys is obtained. A demonstration of the model is given by its application to eutectic tin–lead solder.

First, in Section 2, the phase field model will be introduced which is used to calculate the distribution of the phases in the system. Next, the viscoplastic material model used for each of the individual phases is treated in Section 3, followed by some aspects of the numerical implementation in Section 4. Section 5 deals with the choice of the material parameters. In Section 6 numerical simulations of mechanical loading of a Sn–Pb solder alloy with different microstructure and strain rates are discussed, after which the conclusions will be presented in Section 7.

In the following definitions, a Cartesian basis $\{\vec{e}_1, \vec{e}_2, \vec{e}_3\}$ is used. The Einstein summation convention is adopted, where repeated indices are summed from 1 to 3. Notations and definitions as they are used in this paper are summarised below.

Quantities
Scalar α; a; A
Vector $\vec{a} = a_i\vec{e}_i$
Second order tensor $\boldsymbol{A} = A_{ij}\vec{e}_i\vec{e}_j$
Identity tensor $\boldsymbol{I} = \delta_{ij}\vec{e}_i\vec{e}_j$
Fourth order identity tensor $\mathbb{I} = \delta_{il}\delta_{jk}\vec{e}_i\vec{e}_j\vec{e}_k\vec{e}_l \rightarrow \mathbb{I} : \boldsymbol{A} = \boldsymbol{A}$
Fourth order tensor $\mathbb{A} = A_{ijkl}\vec{e}_i\vec{e}_j\vec{e}_k\vec{e}_l$
Column $\underset{\sim}{a}$
Matrix $\underline{\underline{A}}$

Operations
Scalar multiplication $c = ab$; $\vec{c} = a\vec{b}$; $\boldsymbol{C} = a\mathbf{B}$
Dyadic product $\vec{a} \otimes \vec{b} = a_ib_j\vec{e}_i\vec{e}_j$
Inner product $c = \vec{a} \cdot \vec{b} = a_ib_i$; $\boldsymbol{C} = \boldsymbol{A} \cdot \boldsymbol{B} = A_{ij}B_{jk}\vec{e}_i\vec{e}_k$
Double inner product $c = \boldsymbol{A}{:}\boldsymbol{B} = A_{ij}\,\mathrm{B}_{ji}$; $\boldsymbol{C} = \mathbb{A} : \boldsymbol{B} = A_{ijkl}B_{lk}\vec{e}_i\vec{e}_j$
Conjugate/transpose $\boldsymbol{C}^{\mathrm{c}} = C_{ji}\vec{e}_i\vec{e}_j$; $\mathbb{C}^{\mathrm{c}} = C_{jilk}\vec{e}_i\vec{e}_j\vec{e}_k\vec{e}_l$
Right conjugate $\mathbb{C}^{\mathrm{rc}} = C_{ijlk}\vec{e}_i\vec{e}_j\vec{e}_k\vec{e}_l$
Inverse $\boldsymbol{A}^{-1}$
Determinant $\det(\boldsymbol{A}) = (\boldsymbol{A} \cdot \vec{e}_1) \cdot (\boldsymbol{A} \cdot \vec{e}_2) \times (\boldsymbol{A} \cdot \vec{e}_3)$
Deviatoric part $\boldsymbol{A}^{\mathrm{d}} = \boldsymbol{A} - \frac{1}{3}\boldsymbol{A} : \boldsymbol{I}$
Gradient operator $\vec{\nabla} = \vec{e}_i\frac{\partial}{\partial x_i}$
Laplacian $\nabla^2 = \vec{\nabla} \cdot \vec{\nabla} = \vec{e}_i\frac{\partial}{\partial x_i}\left(\vec{e}_i\frac{\partial}{\partial x_i}\right)$
Derivative $\delta A_{ij} = \frac{\partial A_{ij}}{\partial \delta B_{kl}}\delta B_{lk}\vec{e}_i\vec{e}_j$

2. Phase field model

In order to describe the microstructure and its evolution a phase field model is used. The mass fraction c is taken as the field variable, and it is assumed that it varies continuously throughout the system. The evolution of the mass fraction field is obtained by solving the nonlinear diffusion equation:

$$\rho\frac{\mathrm{d}c}{\mathrm{d}t} = \vec{\nabla} \cdot \rho\boldsymbol{M} \cdot \vec{\nabla}\frac{\delta F}{\delta c}, \tag{1}$$

where ρ is the mass density, t is time, $\boldsymbol{M}$ the mobility tensor and F the free energy. The variation of the free energy with respect to the mass fraction is the chemical potential and is the driving force behind the diffusion process: it determines how the microstructure will evolve. For the moment the free energy is assumed

to consist out of two parts: the configurational energy, which determines the equilibrium mass fractions for the different phases, and the interface energy which controls the number of interfaces, their size, and orientation.

The free energy function which is the starting point for finding an expression for the mass flux is taken from Giacomin and Lebowitz (1997), who derived a macroscopic equation describing phase segregation in microscopic model systems with long-range interactions evolving according to stochastic Kawasaki dynamics with nearest neighbour exchanges (see also Brandon (1994)). They obtained the following expression for the specific free energy:

$$F = F_0(c(\vec{x})) + \frac{1}{4}\int_{\Omega} g(\vec{y})[c(\vec{x}) - c(\vec{x}+\vec{y})]^2 \,\mathrm{d}\vec{y}, \tag{2}$$

where Ω is the region around the material point with position vector $\vec{x}$, $\vec{y}$ a local coordinate vector with respect to $\vec{x}$ pointing to points in Ω, g is the nonlocal kernel (a symmetric smooth function (C^∞)), and F_0 is the equilibrium free energy density of a homogeneous system. Similar nonlocal extensions of the free energy have been used by Gajewski and Zacharias (2003) and Fosdick and Mason (1998).

In this work the introduced nonlocality which accounts for interfacial effects is assumed to be Lagrangian (material) in nature, i.e. the volume over which long range interactions occur is defined by the material configuration. Using the specific free energy (2) and taking the variation with respect to $c(\vec{x})$ in order to obtain the chemical potential μ then gives:

$$\mu = \frac{\delta F}{\delta c(\vec{x})} = \frac{\partial F_0}{\partial c} + \frac{1}{2}\int_{\Omega_0} g(\vec{y})[c(\vec{x}) - c(\vec{x}+\vec{y})]\,\mathrm{d}\vec{y}, \tag{3}$$

which can be rewritten to yield:

$$\mu = \frac{\partial F_0}{\partial c} + \kappa[c(\vec{x}) - \bar{c}(\vec{x})], \tag{4}$$

where κ is the interface tension coefficient. In here, the nonlocal mass fraction $\bar{c}$ is defined as

$$\bar{c}(\vec{x}) = \int_{\Omega_0} g'(\vec{y})c(\vec{x}+\vec{y})\,\mathrm{d}\vec{y}, \quad \kappa = \frac{1}{2}\int_{\Omega_0} g(\vec{y})\,\mathrm{d}\vec{y}, \quad \text{and} \quad g' = g/\kappa. \tag{5}$$

Eq. (5) can be reformulated towards an implicit Helmholtz equation (Ubachs et al., 2004):

$$\bar{c} - \ell^2\nabla_0^2\bar{c} = c, \tag{6}$$

where ∇_0^2 represents Laplacian taken in the material (Lagragian) configuration, and ℓ is an internal length parameter, which, when using an isotropic weighting function, which is only dependent on a radial coordinate r, is defined as

$$\ell^2 = \frac{1}{2\Omega}\int_{\Omega_0} r^2 g(r)\,\mathrm{d}r. \tag{7}$$

Note that the solution of this partial differential equation indeed leads to a strongly nonlocal solution as assumed in (5). Details on this particular topic have been elaborated within the context of strongly nonlocal damage (Peerlings et al., 2001). Details on the explicit format of the nonlocal kernel (which is the result of the adopted mathematical approximation) can be found in this reference as well.

The reformulation of the integral expression (5) into differential equation (6) requires the introduction of boundary conditions. Either the value of $\bar{c}$, its normal derivative, or a linear combination of these quantities must be specified on the boundary. Here the homogeneous Neumann boundary condition has been used:

$$\vec{\nabla}_0\bar{c}\cdot\vec{n} = 0, \tag{8}$$

where $\vec{n}$ is the normal vector of the boundary. This condition preserves the global mass fraction of the entire system in the nonlocal averaging:

$$c_{\text{total}} = \frac{1}{\Omega_0}\int_{\Omega_0} c\,\mathrm{d}\vec{x} = \frac{1}{\Omega_0}\int_{\Omega_0} \bar{c}\,\mathrm{d}\vec{x}. \tag{9}$$

More comments on this boundary condition can be found in Peerlings et al. (2001). The complete nonlocal phase field model now reads

$$\rho\frac{\mathrm{d}c}{\mathrm{d}t} = \vec{\nabla}\cdot\rho\boldsymbol{M}\cdot\vec{\nabla}\left(\frac{\partial F_0}{\partial c} - \kappa(\bar{c}-c)\right), \tag{10}$$

$$\bar{c} - \ell^2\nabla_0^2\bar{c} = c. \tag{11}$$

More information on the diffusional phase field model can be found in Ubachs et al. (2003, 2004).

The solution of the system of equations yields detailed information on the distribution of phases in the material, the position and orientation of interfaces, and the mass fractions in the separate phases. The mechanical behaviour of the material is dependent on its microstructure. The various phases have different mechanical properties and therefore stresses and strains will not be homogeneous throughout the material. Knowledge of the mass fraction field allows to account for the heterogeneity of the material. The differences in constitutive behaviour of the varies phases and interfaces can be dealt with in a continuum manner.

The eutectic tin–lead system is used to demonstrate the suggested approach. The same constitutive model is assumed for both the Pb-rich α-phase and the Sn-rich β-phase. However, the parameters used are different for each phase.

3. Single phase modelling by hyperelasto-viscoplasticity

3.1. Kinematics

Transformation from the undeformed configuration at time t_0 to the current configuration at time t is described by the standard deformation gradient tensor $\boldsymbol{F}$, who's determinant $J = \det(\boldsymbol{F})$ represents the relative volume change. The conventional multiplicative decomposition is used to split the deformation into an elastic and inelastic (viscoplastic) part, denoted by subscripts e and vp respectively:

$$\boldsymbol{F} = (\vec{\nabla}_0\vec{x})^{\mathrm{c}} = \boldsymbol{F}_{\mathrm{e}}\cdot\boldsymbol{F}_{\mathrm{vp}}. \tag{12}$$

The right and left Cauchy–Green strain tensors, $\boldsymbol{C}$ and $\boldsymbol{B}$, and the Green–Lagrange strain tensor $\boldsymbol{E}$ are classically given by

$$\boldsymbol{C} = \boldsymbol{F}^{\mathrm{c}}\cdot\boldsymbol{F}, \quad \boldsymbol{B} = \boldsymbol{F}\cdot\boldsymbol{F}^{\mathrm{c}}, \quad \text{and} \quad \boldsymbol{E} = \frac{1}{2}(\boldsymbol{C}-\boldsymbol{I}). \tag{13}$$

Material velocity is taken into account by the deformation rate and spin tensors $\boldsymbol{D}$ and $\boldsymbol{\Omega}$, the symmetric and skewsymmetric parts of the velocity gradient tensor $\boldsymbol{L}$, respectively. Decomposition (12) implies the introduction of elastic and viscoplastic rate tensors:

$$\boldsymbol{L} = (\vec{\nabla}\vec{v})^{\mathrm{c}} = \dot{\boldsymbol{F}}\cdot\boldsymbol{F}^{-1} = \dot{\boldsymbol{F}}_{\mathrm{e}}\cdot\boldsymbol{F}_{\mathrm{e}}^{-1} + \boldsymbol{F}_{\mathrm{e}}\cdot\dot{\boldsymbol{F}}_{\mathrm{vp}}\cdot\boldsymbol{F}_{\mathrm{vp}}^{-1}\cdot\boldsymbol{F}_{\mathrm{e}}^{-1} = \boldsymbol{L}_{\mathrm{e}} + \boldsymbol{L}_{\mathrm{vp}} = (\boldsymbol{D}_{\mathrm{e}} + \boldsymbol{\Omega}_{\mathrm{e}}) + (\boldsymbol{D}_{\mathrm{vp}} + \boldsymbol{\Omega}_{\mathrm{vp}}). \tag{14}$$

To make the decomposition unique it is commonly assumed that the viscoplastic spin $\boldsymbol{\Omega}_{\mathrm{vp}}$ is zero.

3.2. The Perzyna model

The one-dimensional mechanical representation of the elasto-viscoplastic Perzyna model consists of a spring, a linear viscous dashpot, a hardening spring and a friction slider, see Fig. 1. The elastic spring represents the elastic part of the material response. The viscoplastic response, represented by the viscous dashpot and the (nonlinear) hardening spring becomes manifest as soon as the stress exceeds a characteristic value and the plastic slider gives way.

For the three-dimensional case, the material is assumed to behave viscoplasticly after an equivalent stress measure exceeds the current yield stress τ_y. Here the Von Mises equivalent stress is used which reads in terms of the Kirchhoff stress tensor $\boldsymbol{\tau}$:

$$\tau_{eq} = \sqrt{\frac{3}{2}\boldsymbol{\tau}^{d} : \boldsymbol{\tau}^{d}}, \tag{15}$$

with $\boldsymbol{\tau}^{d}$ the deviatoric part of the stress tensor. The evaluation of the occurrence of yield is commonly evaluated through a yield criterion φ. It can be represented as a yield surface in stress space. The classical Von Mises–Huber yield function φ is used to evaluate the stress state and to check whether the deformation is purely elastic ($\varphi < 0$) or viscoplastic ($\varphi \geqslant 0$):

$$\varphi(\boldsymbol{\tau}, \varepsilon_{vp}) = \tau_{eq} - \tau_y(\tau_{y0}, \varepsilon_{vp}, \dot{\varepsilon}_{vp}). \tag{16}$$

Here, τ_y accounts for linear or nonlinear hardening or softening laws. The initial yield stress is denoted by τ_{y0} while the hardening behaviour will be related to the effective viscoplastic strain measure ε_{vp} and its rate $\dot{\varepsilon}_{vp}$. The effective viscoplastic strain is obtained through integration over the loading history of its time derivative:

$$\varepsilon_{vp} = \int_0^t \dot{\varepsilon}_{vp}\, dt. \tag{17}$$

3.3. Hyperelastic model

A hyperelastic model is chosen to correctly describe the elastic part of the material behaviour at finite deformations. In that case it is assumed that an elastic strain energy function $F_e(\boldsymbol{E})$ exists, which can be

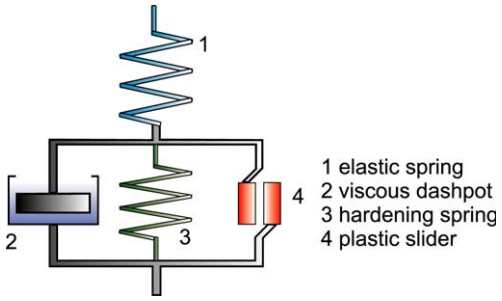

Fig. 1. Schematic one-dimensional representation of the elasto-viscoplastic Perzyna model.

used to calculate the stresses. Here we use it to relate the 2nd Piola–Kirchhoff stress tensor $\boldsymbol{S}$ to the right Cauchy–Green strain tensor $\boldsymbol{C}$:

$$\boldsymbol{S} = J\boldsymbol{F}^{-1}\cdot\boldsymbol{\sigma}\cdot\boldsymbol{F}^{-c} = \boldsymbol{F}^{-1}\cdot\boldsymbol{\tau}\cdot\boldsymbol{F}^{-c} = \frac{\partial F_e}{\partial \boldsymbol{E}} = 2\frac{\partial F_e}{\partial \boldsymbol{C}}, \tag{18}$$

where $\boldsymbol{\sigma}$ is the Cauchy stress tensor. Since the elastic part of the constitutive model is needed in rate form, differentiation with respect to time is performed, yielding

$$\dot{\boldsymbol{S}} = 2\frac{\partial^2 F_e}{\partial \boldsymbol{C}^2} : \dot{\boldsymbol{C}}. \tag{19}$$

An elastic energy function is adopted, which characterises isotropic, compressible material behaviour (Perić, 1992):

$$F_e = \frac{1}{2}\mu[\boldsymbol{C} : \boldsymbol{I} - 3 - 2\ln(J)] + \frac{1}{2}\lambda\ln^2(J), \tag{20}$$

where μ and λ are Lamé's constants defined as

$$\mu = \frac{E}{2(1+v)}, \quad \lambda = \frac{vE}{(1+v)(1-2v)}, \tag{21}$$

with E and v the Young's modulus and Poisson's ratio respectively. The first derivative of Eq. (20) with respect to $\boldsymbol{C}$ then becomes

$$\frac{\partial F_e}{\partial \boldsymbol{C}} = \frac{1}{2}\mu(\boldsymbol{I} - \boldsymbol{C}^{-1}) + \frac{1}{2}\lambda\ln(J)\boldsymbol{C}^{-1}, \tag{22}$$

and its second derivative

$$\frac{\partial^2 F_e}{\partial \boldsymbol{C}^2} = \frac{1}{2}(\mu - \lambda\ln(J))\boldsymbol{C}^{-1}\cdot\mathbb{I}^{rc}\cdot\boldsymbol{C}^{-1} + \frac{1}{4}\lambda\boldsymbol{C}^{-1}\boldsymbol{C}^{-1}. \tag{23}$$

Here use has been made of the following tensor identity:

$$\frac{\partial \boldsymbol{C}^{-1}}{\partial \boldsymbol{C}} = -\boldsymbol{C}^{-1}\cdot\mathbb{I}^{rc}\cdot\boldsymbol{C}^{-1}. \tag{24}$$

3.4. Viscoplastic model

During viscoplastic deformation the yield stress will change as a function of the effective viscoplastic strain. Plastic flow does not induce any stresses in the material, therefore the constitutive model becomes

$$\dot{\boldsymbol{S}} = 2\frac{\partial^2 F_e}{\partial \boldsymbol{C}^2} : (\dot{\boldsymbol{C}} - \dot{\boldsymbol{C}}_{vp}), \tag{25}$$

with

$$\dot{\boldsymbol{C}} = \dot{\boldsymbol{C}}_e + \dot{\boldsymbol{C}}_{vp} = 2\boldsymbol{F}^c\cdot\boldsymbol{D}\cdot\boldsymbol{F}, \tag{26}$$

$$\dot{\boldsymbol{C}}_e = \boldsymbol{F}^c_{vp}\cdot\dot{\boldsymbol{F}}^c_e\cdot\boldsymbol{F}_e\cdot\boldsymbol{F}_{vp} + \boldsymbol{F}^c_{vp}\cdot\boldsymbol{F}^c_e\cdot\dot{\boldsymbol{F}}_e\cdot\boldsymbol{F}_{vp} = 2\boldsymbol{F}^c\cdot\boldsymbol{D}_e\cdot\boldsymbol{F}, \tag{27}$$

$$\dot{\boldsymbol{C}}_{vp} = \dot{\boldsymbol{F}}^c_{vp}\cdot\boldsymbol{F}^c_e\cdot\boldsymbol{F}_e\cdot\boldsymbol{F}_{vp} + \boldsymbol{F}^c_{vp}\cdot\boldsymbol{F}^c_e\cdot\boldsymbol{F}_e\cdot\dot{\boldsymbol{F}}_{vp} = 2\boldsymbol{F}^c\cdot\boldsymbol{D}_{vp}\cdot\boldsymbol{F}. \tag{28}$$

With ongoing viscoplastic deformation the direction of the viscoplastic strain rate $\boldsymbol{D}_{\mathrm{vp}}$ is defined by the commonly used normality or associative flow rule which states that the strain rate is directed along the normal to the yield surface and denoted by $\partial\varphi/\partial\boldsymbol{\tau}$. Its length is characterised by the rate of the viscoplastic multiplier $\dot{\gamma}_{\mathrm{vp}}$. Thus the expression for the viscoplastic strain rate can be formulated as (Perzyna, 1985):

$$\boldsymbol{D}_{\mathrm{vp}} = \dot{\gamma}_{\mathrm{vp}}\boldsymbol{N}, \quad \text{where } \boldsymbol{N} = \frac{\partial\varphi}{\partial\boldsymbol{\tau}} = \frac{3}{2}\frac{\boldsymbol{\tau}^{\mathrm{d}}}{\tau_{\mathrm{eq}}}, \text{ and } \dot{\gamma}_{\mathrm{vp}} = \eta\phi(\varphi), \tag{29}$$

with η a fluidity parameter which determines the magnitude of the viscoplastic strain rate and $\phi(\varphi)$ the overstress function. Viscoplastic strains are nonzero only if $\varphi \geqslant 0$, i.e. for stress states on or outside the yield surface. A power law is chosen for the overstress function (Perzyna, 1971):

$$\phi(\varphi) = \left(\frac{\varphi}{\varphi_0}\right)^N = \left(\frac{\tau_{\mathrm{eq}} - \tau_{\mathrm{y}}}{\varphi_0}\right)^N, \tag{30}$$

with N the rate sensitivity parameter and φ_0 is a scaling parameter. Higher values of N reduce sensitivity of the model to differences between strain rate values (Perić, 1993).

The relation between the rate of the hardening variable $\dot{\varepsilon}_{\mathrm{vp}}$ and of the viscoplastic multiplier $\dot{\gamma}_{\mathrm{vp}}$ is set to the straightforward relation:

$$\dot{\varepsilon}_{\mathrm{vp}} = \dot{\gamma}_{\mathrm{vp}} = \sqrt{\frac{2}{3}\boldsymbol{D}_{\mathrm{vp}} : \boldsymbol{D}_{\mathrm{vp}}}. \tag{31}$$

The hyperelastic material model returns the stress when the elastic deformation is known. However, as can be seen again from the mechanical model, the elastic deformation has to be isolated from the total deformation, which is generally known during an analysis. This is only possible if the viscoplastic stress can be evaluated. As is described above, the viscoplastic strain rate is related to the stress by the flow rule. An integration procedure is needed to calculate the viscoplastic strain.

In case of viscoplastic behaviour, i.e. $\varphi \geqslant 0$ the model now consists of the following system of equations:

$$\dot{\boldsymbol{S}} = 2\frac{\partial^2 F_{\mathrm{e}}}{\partial \boldsymbol{C}^2} : (\dot{\boldsymbol{C}} - \dot{\boldsymbol{C}}_{\mathrm{vp}}), \quad \text{with } \dot{\boldsymbol{C}}_{\mathrm{vp}} = 2\boldsymbol{F}^{\mathrm{c}} \cdot \dot{\gamma}_{\mathrm{vp}}\boldsymbol{N} \cdot \boldsymbol{F}, \tag{32a}$$

$$\dot{\gamma}_{\mathrm{vp}} = \eta\left(\frac{\tau_{\mathrm{eq}} - \tau_{\mathrm{y}}}{\varphi_0}\right)^N. \tag{32b}$$

In case of fully elastic behaviour, i.e. $\varphi < 0$, $\dot{\gamma}_{\mathrm{vp}}$ will equal zero and only Eq. (32a) needs to be solved.

3.5. Phase field coupling

As mentioned earlier each phase is assumed to obey the same constitutive law, only the parameters differ. This means that the elastically and viscoplastically stored energy F_{e} and F_{vp} are dependent on the mass fraction c. In this way information on the microstructure obtained with the phase field model is included in the constitutive model. In their turn, the mechanically stored energies will influence the phase field and its evolution. The chemical potential now reads

$$\mu = \frac{\partial F_0}{\partial c} + \frac{\partial F_{\mathrm{e}}}{\partial c} + \frac{\partial F_{\mathrm{vp}}}{\partial c} + \kappa[c - \bar{c}]. \tag{33}$$

However, in this contribution the microstructure evolution is evaluated separately from the mechanical part of the model. Therefore, the influence of the mechanically stored energies on the diffusion is not taken into account.

4. Finite element implementation

4.1. Momentum equation

In the absence of body/volumetric forces, the momentum equation is given by the zero divergence of the Cauchy stress tensor:

$$\vec{\nabla} \cdot \boldsymbol{\sigma} = 0. \tag{34}$$

The gradient operator in this equation is the spatial, or Eulerian gradient operator, i.e. it is taken in the current configuration. Multiplying the equation with a vectorial weighting function $\vec{w}$ and integrating over the domain Ω with a boundary Γ whose unit outward normal is $\vec{n}$, yields

$$\int_{\Omega} \vec{w} \cdot (\vec{\nabla} \cdot \boldsymbol{\sigma}) \, \mathrm{d}\Omega = 0, \quad \forall \vec{w}. \tag{35}$$

Applying the divergence theorem, using $\boldsymbol{\sigma} = \boldsymbol{\sigma}^c$ and applying the natural boundary condition $\boldsymbol{\sigma} \cdot \vec{n} = \vec{p}$ on Γ leads to

$$\int_{\Omega} (\vec{\nabla}\vec{w})^{\mathrm{c}} : \boldsymbol{\sigma} \, \mathrm{d}\Omega = \int_{\Gamma} \vec{w} \cdot \vec{p} \, \mathrm{d}\Gamma. \tag{36}$$

Because of the nonlinear and time dependent nature of the stress this equation needs to be solved iteratively by using a standard Newton–Raphson iteration procedure. First the left hand side is transformed to the last known equilibrium configuration at time t according to $\vec{\nabla} = \boldsymbol{F}_{\Delta}^{-\mathrm{c}} \cdot \vec{\nabla}_t$ (with $\boldsymbol{F}_{\Delta} = \boldsymbol{F} \cdot [\boldsymbol{F}^t]^{-1}$ the incremental deformation gradient tensor) and $\mathrm{d}\Omega = (J/J^t)\,\mathrm{d}\Omega^t$, and using $\boldsymbol{\tau} = J\boldsymbol{\sigma}$ results in

$$\int_{\Omega^t} (\vec{\nabla}_t \vec{w})^{\mathrm{c}} : \boldsymbol{F}_{\Delta}^{-1} \cdot \boldsymbol{\tau} \frac{1}{J^t} \, \mathrm{d}\Omega^t = \int_{\Gamma} \vec{w} \cdot \vec{p} \, \mathrm{d}\Gamma. \tag{37}$$

Next, the unknown Kirchhoff stress tensor and incremental deformation gradient tensor are decomposed in an iterative manner,

$$\boldsymbol{\tau} = \boldsymbol{\tau}^{(i+1)} = \boldsymbol{\tau}^{(i)} + \delta\boldsymbol{\tau} \quad \wedge \quad \boldsymbol{F}_{\Delta} = \boldsymbol{F}_{\Delta}^{(i+1)} = \boldsymbol{F}_{\Delta}^{(i)} + \delta\boldsymbol{F}_{\Delta}, \tag{38}$$

leading to the following linearised weak formulation of the equilibrium condition

$$\begin{aligned} \int_{\Omega^t} [(\vec{\nabla}_t \vec{w})^{\mathrm{c}} : (\delta[\boldsymbol{F}_{\Delta}^{-1}] \cdot \boldsymbol{\tau}^{(i)} + [\boldsymbol{F}_{\Delta}^{(i)}]^{-1} \cdot \delta\boldsymbol{\tau})] \frac{1}{J^t} \mathrm{d}\Omega^t = \int_{\Gamma} \vec{w} \cdot \vec{p}^{(i+1)} \, \mathrm{d}\Gamma - \int_{\Omega^t} (\vec{\nabla}_t \vec{w})^{\mathrm{c}} \\ : ([\boldsymbol{F}_{\Delta}^{(i)}]^{-1} \cdot \boldsymbol{\tau}^{(i)}) \frac{1}{J^t} \mathrm{d}\Omega^t. \end{aligned} \tag{39}$$

Introducing the variational deformation gradient tensor

$$\boldsymbol{L}_{\delta}^{\mathrm{c}} = (\vec{\nabla}\delta\vec{x})^{\mathrm{c}} = \delta\boldsymbol{F} \cdot \boldsymbol{F}^{-1} = \delta\boldsymbol{F}_{\Delta} \cdot \boldsymbol{F}_{\Delta}^{-1}, \tag{40}$$

allows for rewriting $\delta[\boldsymbol{F}_{\Delta}^{-1}]$ as $-[\boldsymbol{F}_{\Delta}^{(i)}]^{-1} \cdot \delta\boldsymbol{F}_{\Delta} \cdot [\boldsymbol{F}_{\Delta}^{(i)}]^{-1} = -[\boldsymbol{F}_{\Delta}^{(i)}]^{-1} \cdot \boldsymbol{L}_{\delta}^{\mathrm{c}}$. Transformation back to the last known configuration then results in

$$\int_{\Omega} (\vec{\nabla}\vec{w})^{\mathrm{c}} : [-\mathbb{I} \cdot \boldsymbol{\tau}^{(i)} : \boldsymbol{L}_{\delta}^{\mathrm{c}} + \delta\boldsymbol{\tau}] \frac{1}{J^{(i)}} \, \mathrm{d}\Omega = \int_{\Gamma} \vec{w} \cdot \vec{p}^{(i+1)} \, \mathrm{d}\Gamma - \int_{\Omega} (\vec{\nabla}\vec{w})^{\mathrm{c}} : \boldsymbol{\tau}^{(i)} \frac{1}{J^{(i)}} \, \mathrm{d}\Omega. \tag{41}$$

4.2. Incremental time discretisation

To solve Eq. (41), an expression for the Kirchhoff stress tensor is needed. It can be derived from the constitutive equations, system (32). Since this system cannot be integrated analytically, an incremental time integration scheme will be used. The system is formulated in terms of invariant variables, which remain unaltered under superposed spatial rigid body motions thereby preserving the principle of objectivity. This ensures that no spurious stresses are generated due to rigid body motions. An implicit (or backward) Euler scheme is used, resulting in

$$\Delta \boldsymbol{S} = \boldsymbol{S} - \boldsymbol{S}^t = 2\frac{\partial^2 F_e}{\partial \boldsymbol{C}^2} : (\boldsymbol{C} - \boldsymbol{C}^t - 2\boldsymbol{F}^c \cdot \Delta\gamma_{vp}\boldsymbol{N} \cdot \boldsymbol{F}), \tag{42a}$$

$$\Delta\gamma_{vp} = \gamma_{vp} - \gamma_{vp}^t = \Delta t\eta\left(\frac{\tau_{eq} - \tau_y}{\varphi_0}\right)^N, \tag{42b}$$

which can be rewritten in terms of the Kirchhoff stress by applying a push forward towards the current configuration yielding

$$\boldsymbol{\tau} = \boldsymbol{F}_{\Delta} \cdot \boldsymbol{\tau}^t \cdot \boldsymbol{F}_{\Delta}^c + \mathbb{H} : [\boldsymbol{e}_{\Delta} - \Delta\gamma_{vp}\boldsymbol{N}], \tag{43a}$$

$$\Delta\gamma_{vp} = \Delta t\eta\left(\frac{\varphi}{\varphi_0}\right)^N, \tag{43b}$$

where $\boldsymbol{e}_{\Delta}$ is the incremental Almansi strain tensor

$$\boldsymbol{e}_{\Delta} = \frac{1}{2}\left(\boldsymbol{I} - \boldsymbol{F}_{\Delta}^{-c} \cdot \boldsymbol{F}_{\Delta}^{-1}\right), \tag{44}$$

and $\mathbb{H}$ represents the fourth order constitutive tensor

$$\mathbb{H} = 4\left[\boldsymbol{F} \cdot \left(\boldsymbol{F} \cdot \frac{\partial^2 F_e}{\partial \boldsymbol{C}^2} \cdot \boldsymbol{F}^c\right)^{lc,rc} \cdot \boldsymbol{F}^c\right]. \tag{45}$$

Substituting Eq. (23) this can be rewritten to yield

$$\mathbb{H} = 2[\mu - \lambda \ln(J)]\mathbb{I}^{rc} + \lambda \boldsymbol{II}. \tag{46}$$

It now remains to relate the variation of the Kirchhoff stress Eq. (43)to $\boldsymbol{L}_{\delta}^c$:

$$\delta\boldsymbol{\tau} = \mathbb{C} : \boldsymbol{L}_{\delta}^c. \tag{47}$$

In the following section the consistent tangents will be derived for the elastic and the viscoplastic case.

4.3. Consistent tangent

For a fully elastic increment, i.e. $\varphi < 0$ the incremental update for the Kirchhoff stress tensor reads:

$$\boldsymbol{\tau} = \boldsymbol{F}_{\Delta} \cdot \boldsymbol{\tau}^t \cdot \boldsymbol{F}_{\Delta}^c + \mathbb{H}(J) : \boldsymbol{e}_{\Delta}. \tag{48}$$

The variation of the stress then becomes:

$$\delta\boldsymbol{\tau} = \delta\boldsymbol{F}_{\Delta} \cdot \boldsymbol{\tau}^t \cdot \boldsymbol{F}_{\Delta}^c + \boldsymbol{F}_{\Delta} \cdot \boldsymbol{\tau}^t \cdot \delta\boldsymbol{F}_{\Delta}^c + \frac{\partial \mathbb{H}}{\partial J} : \boldsymbol{e}_{\Delta}\delta J + \mathbb{H}(J) : \delta\boldsymbol{e}_{\Delta}, \tag{49}$$

which after some manipulations, see Appendix A.1, can be rewritten in the form of Eq. (47) with

$$\mathbb{C} = \mathbb{C}_e = 2\mathbb{I}^S \cdot \boldsymbol{F}_\Delta \cdot \boldsymbol{\tau}^t \cdot \boldsymbol{F}_\Delta^c + J\frac{\partial \mathbb{H}}{\partial J} : \boldsymbol{e}_\Delta \boldsymbol{I} + \mathbb{H} : \left(\mathbb{I}^S \cdot \boldsymbol{F}_\Delta^{-c} \cdot \boldsymbol{F}_\Delta^{-1}\right)^{rc}. \tag{50}$$

The derivative of the material tensor $\mathbb{H}$, Eq. (46), with respect to J reads

$$\frac{\partial \mathbb{H}}{\partial J} = -2\lambda \frac{\partial \ln(J)}{\partial J}\mathbb{I}^{rc} = -2\lambda \frac{1}{J}\mathbb{I}^{rc}. \tag{51}$$

For a viscoplastic increment ($\varphi > 0$) the incremental update of the Kirchhoff stress tensor reads:

$$\boldsymbol{\tau} = \boldsymbol{F}_\Delta \cdot \boldsymbol{\tau}^t \cdot \boldsymbol{F}_\Delta^c + \mathbb{H}(J) : (\boldsymbol{e}_\Delta - \Delta\gamma_{vp}\boldsymbol{N}). \tag{52}$$

The hardening law is next assumed to be a function of γ_{vp} only, i.e. the yield stress can be a function of the viscoplastic multiplier and/or its rate, $\tau_y(\gamma_{vp}, \dot{\gamma}_{vp})$. After some manipulations, see Appendix A.2, the variation of the stress can be rewritten as

$$\delta\boldsymbol{\tau} = \mathbb{N}^{-1} : (\mathbb{C}_e + \mathbb{T}) : \boldsymbol{L}_\delta^c = \mathbb{C}_{vp} : \boldsymbol{L}_\delta^c, \tag{53}$$

with $\mathbb{C}_e$ as defined in Eq. (50), and the fourth order tensors $\mathbb{T}$ and $\mathbb{N}$ as

$$\mathbb{T} = 2\Delta\gamma_{vp}\lambda\frac{1}{J}\boldsymbol{N}\boldsymbol{I}, \tag{54}$$

and

$$\mathbb{N} = \mathbb{I} + c_2\mathbb{H} : \boldsymbol{N}\boldsymbol{N} + \mathbb{H} : \Delta\gamma_{vp}\frac{1}{\tau_{eq}}\left(\frac{3}{2}\mathbb{I} - \frac{1}{2}\boldsymbol{I}\boldsymbol{I} - \boldsymbol{N}\boldsymbol{N}\right). \tag{55}$$

where the coefficients c_1 and c_2 equal

$$c_1 = N\Delta t\frac{\eta}{\varphi_0}\left(\frac{\tau_{eq} - \tau_y}{\varphi_0}\right)^{N-1} \quad \text{and} \quad c_2 = \frac{c_1}{1 + \frac{\partial \tau_y}{\partial \Delta\gamma_{vp}}c_1}. \tag{56}$$

4.4. Stress update algorithm

Every increment is initially assumed to be fully elastic. The stresses obtained in this elastic predictor state are then used to check the yield criterion. If this has been violated return mapping has to be performed, i.e. the amount and direction of plastic flow has to be determined and the stresses should be updated accordingly. The return mapping requires the set of nonlinear Eqs. (43) to be solved. This will be done using the previously described standard Newton–Raphson iterative procedure.

It can be shown that for the current hyperelastic model the direction of plastic flow is fully determined by the elastic predictor state, $\boldsymbol{N} = {}^*\boldsymbol{N}$, see Appendix A.3. Furthermore, for the stress update algorithm the nodal displacements are known and fixed, except for the plane stress case. Therefore the volume and the stresses of the elastic predictor will not change, i.e. δJ and $\delta^*\tau$ are zero. Decomposing system (43) in an iterative manner, $(\,\cdot\,)^{(i+1)} = (\,\cdot\,) + \delta(\,\cdot\,)$, thus results in

$$\mathbb{I} : \delta\boldsymbol{\tau} + \mathbb{H} : \boldsymbol{N}\delta\Delta\gamma_{vp} = {}^*\boldsymbol{\tau} - \boldsymbol{\tau} - \mathbb{H} : \boldsymbol{N}\Delta\gamma_{vp}, \tag{57a}$$

$$\delta\Delta\gamma_{vp} - c_1(\boldsymbol{N} : \delta\boldsymbol{\tau} - \delta\tau_y) = \Delta t\eta\left(\frac{\varphi}{\varphi_0}\right)^N - \Delta\gamma_{vp}, \tag{57b}$$

with

$$c_1 = \frac{\Delta t \eta N}{\varphi_0}\left(\frac{\varphi}{\varphi_0}\right)^{N-1}. \tag{58}$$

See Appendix A.3 for details. Since it is assumed that the incremental hardening law is only a function of $\Delta\gamma_{\mathrm{vp}}$ the system that needs to be solved becomes

$$\mathbb{I} : \delta\boldsymbol{\tau} + \mathbb{H} : \boldsymbol{N}\delta\Delta\gamma_{\mathrm{vp}} = {}^{*}\boldsymbol{\tau} - \boldsymbol{\tau} - \mathbb{H} : \boldsymbol{N}\Delta\gamma_{\mathrm{vp}}, \tag{59a}$$

$$-c_1\boldsymbol{N} : \delta\boldsymbol{\tau} + \left(1 + c_1\frac{\partial\tau_{\mathrm{y}}}{\partial\Delta\gamma_{\mathrm{vp}}}\right)\delta\Delta\gamma_{\mathrm{vp}} = \Delta t\eta\left(\frac{\varphi}{\varphi_0}\right)^{N} - \Delta\gamma_{\mathrm{vp}}. \tag{59b}$$

The system can also be solved in an uncoupled manner, first Eq. (43b) is solved, next the stress is updated by evaluating the linear equation (43a). Linearisation of Eq. (43b) yields

$$\left[1 + c_1\left(\boldsymbol{N} : \mathbb{H} : \boldsymbol{N} + \frac{\partial\tau_{\mathrm{y}}}{\partial\Delta\gamma_{\mathrm{vp}}}\right)\right]\delta\Delta\gamma_{\mathrm{vp}} = \Delta t\eta\left(\frac{\varphi}{\varphi_0}\right)^{N} - \Delta\gamma_{\mathrm{vp}}. \tag{60}$$

5. Material parameters

In order to minimize the global energy, a homogeneous tin–lead mixture will start to phase separate. From the free energy function for the system, see Fig. 2, it can be deduced that the preferred state of material is a system consisting of α- and β-phase regions with mass fractions corresponding to the binodal points. In this state the configurational energy of the total system is at its lowest point. The binodal points can be found by constructing a double tangent to the free energy curve. For more details on this subject see Ubachs et al. (2004). It follows that, with the exception of the interfaces, the tin–lead system consists only of α- and β-phase regions, whose compositions are determined by the corresponding binodal points.

No direct mechanical data is available on the separate phases. Therefore, the required parameters are extracted from measurements performed on multiphase solder joints. First the material parameters for the bulk solder are determined. Next, a linear extrapolation is performed to find the required parameters for the α-phase containing 0% Sn and the β-phase containing 0% Pb. To find the material parameters η, N, τ_{y}, and φ_0 for the Perzyna model, saturation stress versus inelastic strain curves are reproduced from the parameters for the Anand model given in Cheng et al. (2000) and Wang et al. (2001) who exploited data provided by Darveaux and Banerji (1992). In the experiments performed by Darveaux and Banerji (1992)

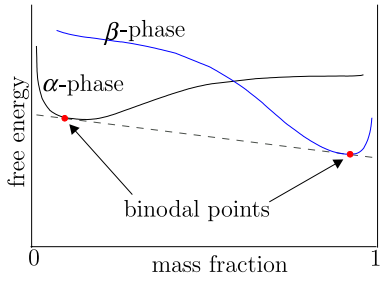

Fig. 2. Configurational free energy for a two phase system.

shear deformations up to 50% for 60Sn–40Pb and 130% for 2.5Sn–97.5Pb were recorded before the onset of damage.

From the experimental stress strain curves at constant strain rates it can be seen that the hardening is strain rate dependent. Therefore the following evolution law for the yield stress is chosen

$$\tau_y = \tau_{y0} + h_1 \dot{\varepsilon}_{vp}^{h_2} [1 - \exp(-h_3 \varepsilon_{vp})], \tag{61}$$

where h_1, h_2, and h_3 are hardening parameters. The derivative of the yield stress with respect to the visco-plastic multiplier needed for Eqs. (60) and (56) then reads (after applying a backward Euler time discretisation)

$$\frac{\partial \tau_y}{\partial \varepsilon_{vp}} \frac{\partial \varepsilon_{vp}}{\partial \Delta \gamma_{vp}} = \frac{h_1}{\Delta t} \dot{\varepsilon}_{vp}^{h_2 - 1} [h_2 - (h_2 - h_3 \Delta \gamma_{vp}) \exp(-h_3 \varepsilon_{vp})]. \tag{62}$$

The parameter determination will be done from stress strain curves obtained at constant strain rates. In that case the following expression for the stress during a uniaxial tensile test at constant strain rate can be found using Eqs. (29)–(31):

$$\tau_{eq} = \varphi_0 \left(\frac{\dot{\varepsilon}_{vp}}{\eta} \right)^{1/N} + \tau_{y0} + h_1 \dot{\varepsilon}_{vp}^{h_2} [1 - \exp(-h_3 \varepsilon_{vp})]. \tag{63}$$

Fig. 3 shows the material data from Cheng et al. (2000) and the fitted curves for two Sn–Pb systems with different mass compositions. First the η, N, τ_{y0}, and φ_0 are determined by fitting. They determine the initial yield stress—indicated in the figures by a circle—which is highly dependent on the strain rate. These parameters are then held constant while the hardening parameters are fitted. The fitted parameters for both compositions are summarised in Table 1.

Because the phase field model provides a continuous field for the mass fraction c ranging from 0 to 1, material parameters need to be known for all $0 \leqslant c \leqslant 1$. In a first-order approximation, all parameters are assumed to be linearly dependent on c, e.g. $E = (1 - c)E_{Pb} + cE_{Sn}$. Parameter values for the individual components should correspond to the parameters found with the fitting procedure above when using this linear rule to calculate properties for their specific composition. This assumption then allows for extracting material parameters for the individual phases. The applied first-order rule is only valid nearby the α and the β phases, which are the phases actually present in the multi-phase mixture. Note that the values for the α-phase with 0% tin (α-0%Sn) and the β-phase containing 0% lead (β-0%Pb) can differ considerably from

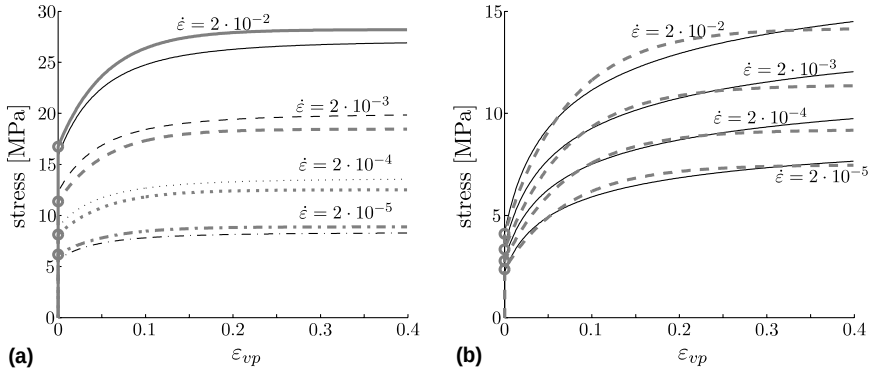

Fig. 3. Fitting of Perzyna parameters, stress versus inelastic strain, dotted lines are fitted: (a) 60Sn–40Pb ($c = 0.6$), (b) 2.5Sn–97.5Pb ($c = 0.025$).

Table 1
Perzyna material data for the tin–lead solder system

Parameter	Symbol	Unit	60–40 tin–lead	0.025–97.5 tin–lead	β-0%Pb	α-0%Sn
Young's modulus	E	[GN/m^2]	10–39		41	16
Poisson's ratio	ν	[−]	0.32–0.37		0.33	0.44
Initial yield stress	τ_{y0}	[MPa]	3.20	1.139	4.637	1.049
Fluidity	η	[−]	1.41×10^{-5}	5.88×10^{-6}	1.98×10^{-5}	5.52×10^{-6}
Rate sensitivity	N	[−]	4.55	7.79	2.30	7.94
Hardening parameter	h_1	[MPa]	29.91	15.83	39.71	15.22
	h_2	[−]	0.208	0.0979	0.285	0.0931
	h_3	[−]	18.41	13.73	21.67	13.53
Thermal expansion coefficient	α	[1/K]			1.67×10^{-5}	2.89×10^{-5}
Density	ρ	[kg/m^3]			7260	11300
Mobility	$\boldsymbol{M}$	[m^5/(J s)]			2.2×10^{-25}	0
Gradient energy coefficient	κ	[GJ/m^3]			16	16
Internal length parameter	ℓ	[nm]			25	25

values for the pure elements, lead and tin. They are however used here only to obtain the correct interpolated values. The parameters as used for the finite element calculations are shown in Table 1.

6. Numerical results

Simulations of mechanical loading have been performed on different microstructures which are assumed not to evolve during the loading. This can be assumed for this particular test since the mechanical time scale is very small compared to the diffusion time scale. The microstructures are obtained by solving the phase field equations discussed in Section 2. Here the results of a simulation for static ageing at 150 °C have been used as microstructural input for the mechanical model. For these calculations the mechanical component of the free energy has been neglected, i.e. mechanical loading is assumed not to influence the diffusion process. The initial conditions for these calculations are taken from a scanning electron micrograph of as-cast eutectic tin–lead solder (Matin et al., 2004). Quantitative comparison between the simulation and the experiment showed a good agreement (Ubachs et al., 2004). Four different microstructures have been subjected to the mechanical loading, immediately after casting (as-cast), indicated as microstructure A and after 2, 6, and 15 h of ageing, respectively indicated as microstructure B, C, and D. They are shown in Fig. 4. The dark regions correspond to the α or Pb-rich phase while the light regions correspond to the β or Sn-rich phase.

The specimens are subjected to cyclic shearing to 2% global deformation after which the direction of shearing is reversed until the 0% shear state is recovered. After three cycles the specimens are held to evaluate the relaxation behaviour. For all the microstructures a strain rate of 2×10^{-3} is used. The calculations

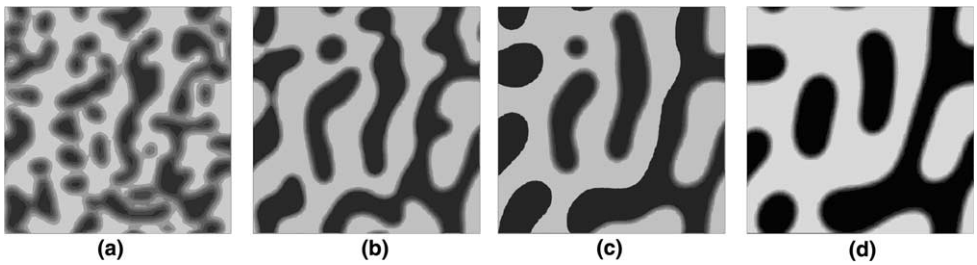

Fig. 4. Microstructure of aged eutectic tin–lead aged at 150 °C: (a) aged for 0 h, (b) aged for 2 h, (c) aged for 6 h, (d) aged for 15 h.

have been performed using periodic boundary conditions: The deformation of each opposing boundary pair is equal and the stress vectors are opposite in sign on each pair (Kouznetsova et al., 2001; Smit et al., 1999). The appropriate dependencies for the edges, see Fig. 5, are:

$$\vec{x}_{\mathrm{R}} - \vec{x}_{\mathrm{BR}} = \vec{x}_{\mathrm{L}} - \vec{x}_{\mathrm{BL}}, \quad \text{and} \quad \vec{x}_{\mathrm{T}} - \vec{x}_{\mathrm{TL}} = \vec{x}_{B} - \vec{x}_{\mathrm{BL}}, \tag{64}$$

where the subscripts L, R, T, and B denote left, right, top, and bottom respectively. A regular mesh of 50 by 50 quadratic elements has been used. In this way each interface is described by approximately 3–4 quadratic elements.

Fig. 6 shows the global reaction force as a function of time for the different microstructures. At first the maximum reaction force increases with each cycle due to hardening of the material, but after a small number of cycles a steady state is reached. This is more clearly depicted in Fig. 7 which shows the reaction force versus displacement curve for 12 shearing cycles performed on microstructure D with $\dot{\varepsilon} = 2 \times 10^{-3}$.

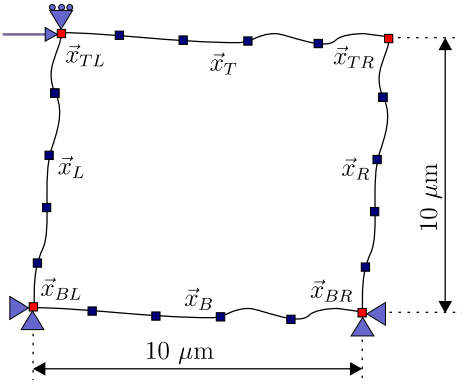

Fig. 5. Periodic mesh and boundary conditions.

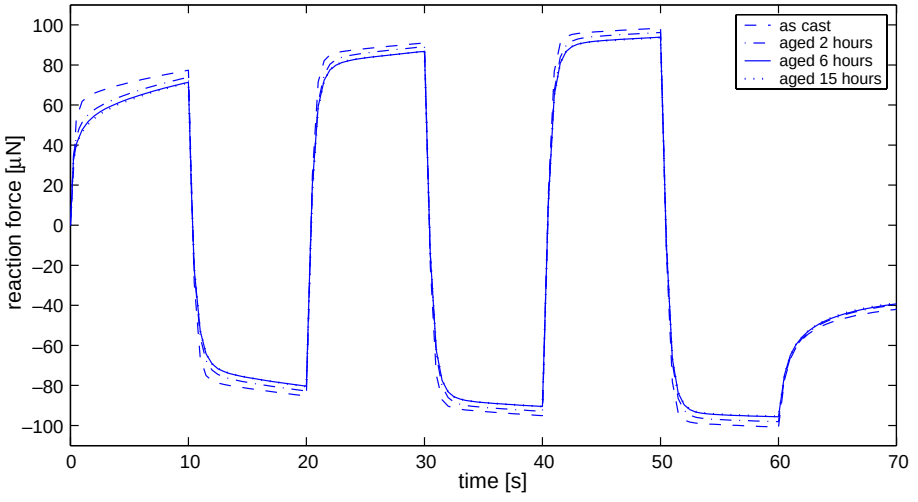

Fig. 6. Reaction force versus time for different microstructures, strain rate 2×10^{-3}.

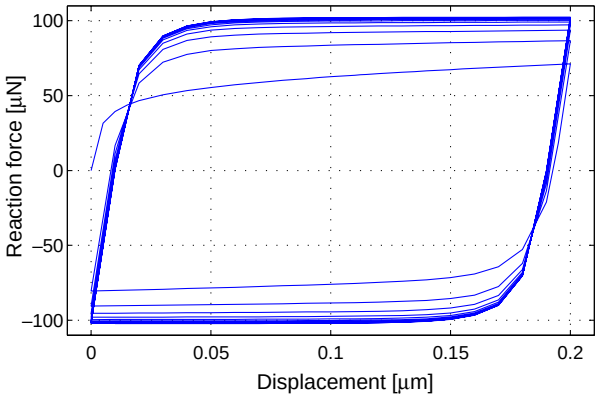

Fig. 7. Reaction force versus displacement, microstructure D, $\dot{\varepsilon} = 2 \times 10^{-3}$.

A dependency on the microstructure can be seen in Fig. 6. Ageing of the material, which leads to an increase of microstructural length scales, results in a lower yield point and lower reaction forces during loading. Microstructure A clearly shows the highest overall reaction force, Microstructures B and C clearly show a consecutive reduction of the reaction forces. However, between microstructures C and D the difference is very small. This can be explained by the fact that relatively little coarsening has occurred in this last stage of the ageing process resulting in similar microstructures.

The tendency 'small is strong' is also known to occur in single phase materials, which show a increasing strength as the grain size decreases. The best-known macroscopic experimental consequence is the increased flow stress on decreasing average grain size, which is expressed by the so-called Hall–Petch relation (Evers et al., 2004). This strengthening effect is commonly attributed to stress concentrations originating from

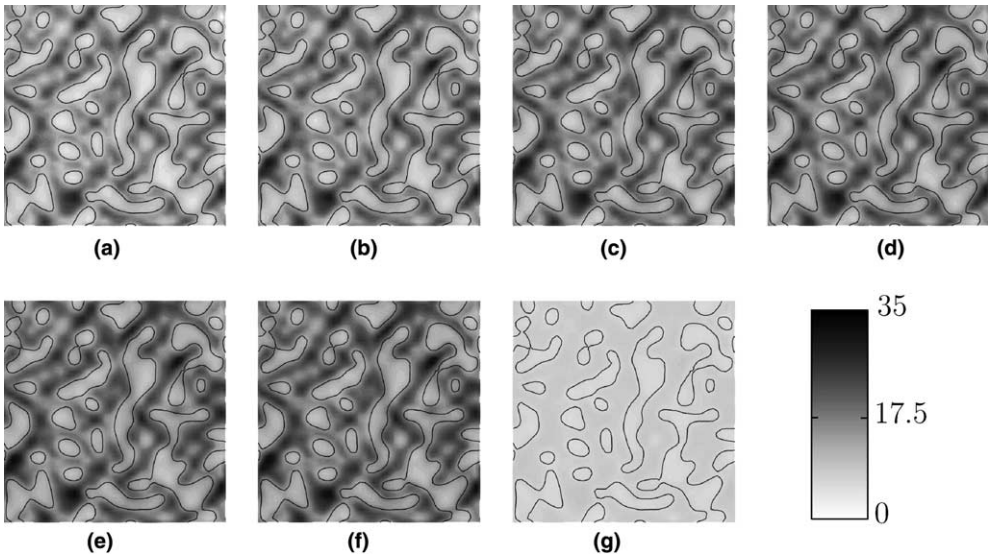

Fig. 8. Evolution of the equivalent Cauchy stress field in MPa for the as-cast microstructure, strain rate 2×10^{-3}: (a) $t = 10$ s, (b) $t = 20$ s, (c) $t = 30$ s, (d) $t = 40$ s, (e) $t = 50$ s, (f) $t = 60$ s, (g) $t = 70$ s.

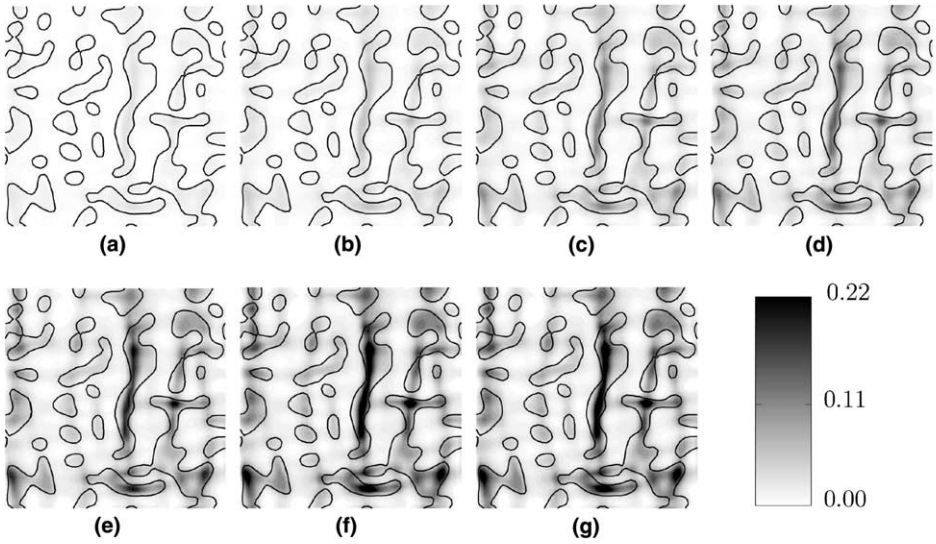

Fig. 9. Evolution of the effective viscoplastic strain field for the as-cast microstructure, strain rate 2×10^{-3}: (a) $t = 10\,\mathrm{s}$, (b) $t = 20\,\mathrm{s}$, (c) $t = 30\,\mathrm{s}$, (d) $t = 40\,\mathrm{s}$, (e) $t = 50\,\mathrm{s}$, (f) $t = 60\,\mathrm{s}$, (g) $t = 70\,\mathrm{s}$.

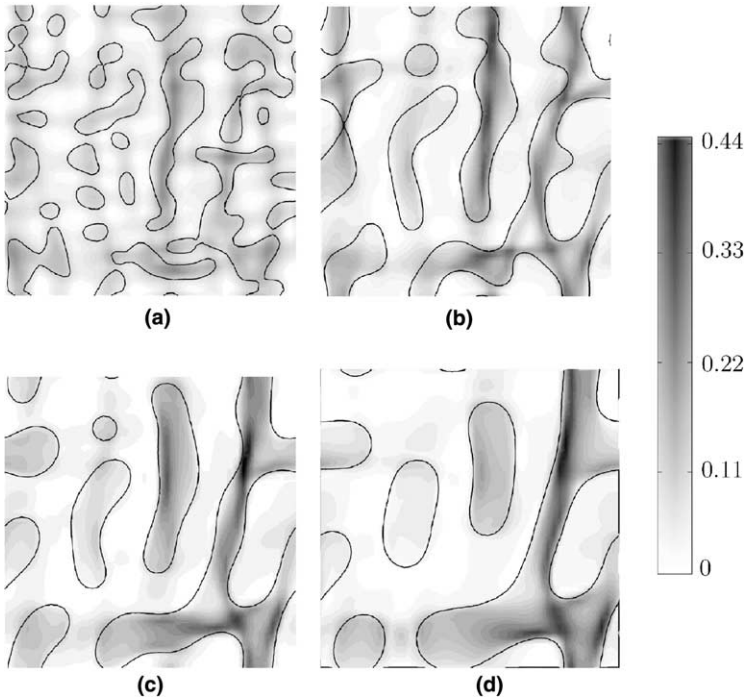

Fig. 10. Equivalent viscoplastic strain at 70 s for the different microstructures, strain rate 2×10^{-3}: (a) aged for 0 h, (b) aged for 2 h, (c) aged for 6 h, (d) aged for 15 h.

material heterogeneity, which obstruct plastic flow. Therefore, next, the strain and stress distributions within the microstructures will be investigated to find the cause behind the strengthening effect found here for the eutectic tin–lead system.

The development of the equivalent Cauchy stress, σ_{eq} for microstructure A ($\dot{\varepsilon} = 2 \times 10^{-3}$) is shown in Fig. 8. It can be clearly seen that stress concentrations develop in the hard β-phase. Since the yield stress is much lower in the α-phase it will start to flow plastically before the yield stress in the rest of the material has been reached. The hardening induced by the plastic flow is not significant enough to smooth the stress field. This can be observed in Fig. 9 which shows the development of the effective viscoplastic strain, ε_{vp}. The plastic strain is almost completely confined to the α-phase. It should be noted that due to the localisation of plastic straining the effective viscoplastic strain reaches values of 0.22 already after 3 cycles, which is much higher than the applied macro shear strain of 0.02. The heterogeneous plastic straining of the material results in residual stresses after relaxation. All the other simulations show the same qualitative behaviour. Therefore the ε_{vp} is only shown at the end of the simulation, Fig. 10, and the σ_{eq} at $t = 60$ and 70 s, that is at maximum stress levels and after relaxation, Figs. 11 and 12.

As opposed to the reaction force, the stress concentrations increase with increasing microstructural sizes. This is due to the fact that the finer microstructure allows for a better distribution of the stresses, whereas the coarser microstructure forces the stresses to localize more. The residual stresses after relaxation do not show a significant difference between the various microstructures. The effect of increasing microstructural length scale can be seen more clearly by comparing the equivalent viscoplastic strain fields, see Fig. 10. Increased ageing, or coarsening, leads to increased localisation behaviour and thus higher (local) values for the viscoplastic strain. Note that the maximum viscoplastic strain is in fact higher for the 6 h aged microstructure than for the 15 h one. This is due to the higher curvature at

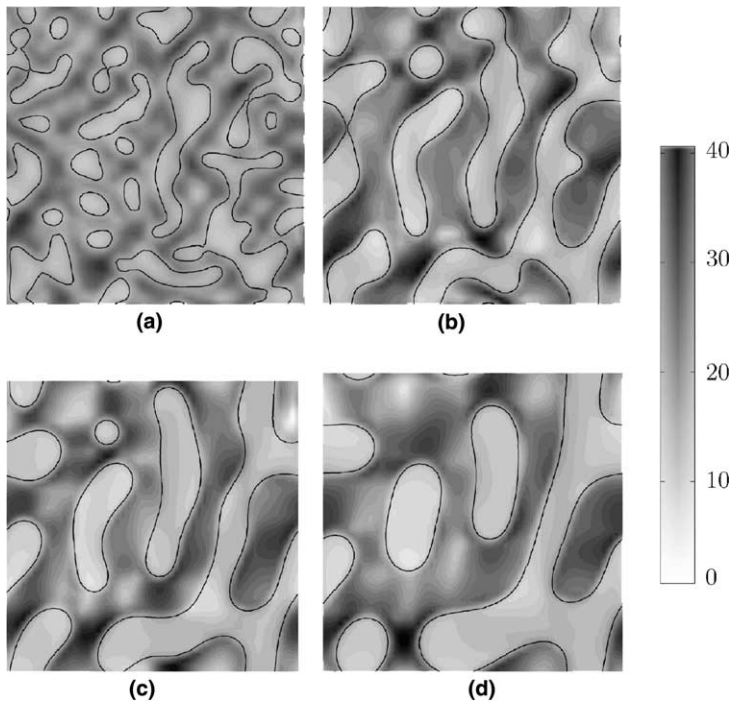

Fig. 11. Equivalent Cauchy stress in MPa at 60 s for different microstructures, strain rate 2×10^{-3}: (a) aged for 0 h, (b) aged for 2 h, (c) aged for 6 h, (d) aged for 15 h.

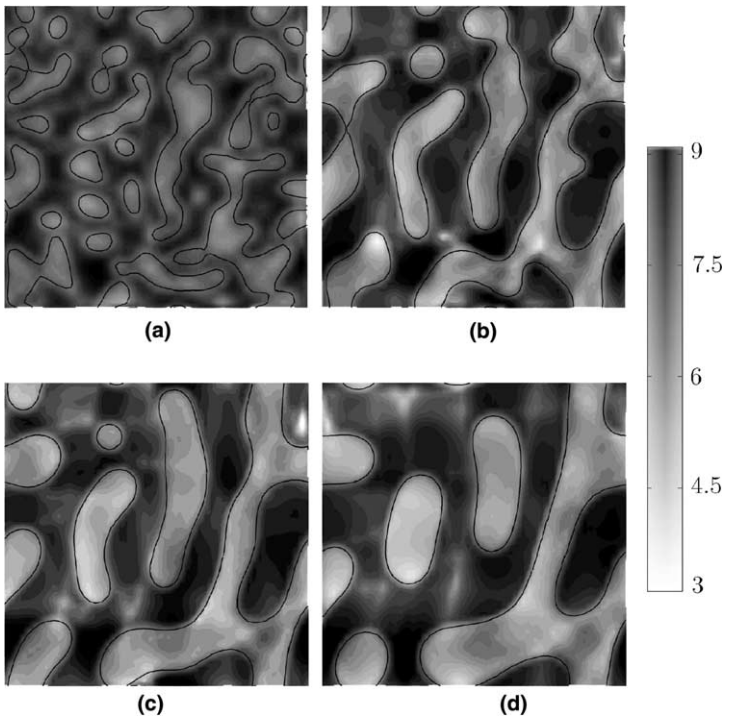

Fig. 12. Equivalent Cauchy stress in MPa at 70 s for different microstructures, strain rate 2×10^{-3}: (a) aged for 0 h, (b) aged for 2 h, (c) aged for 6 h, (d) aged for 15 h.

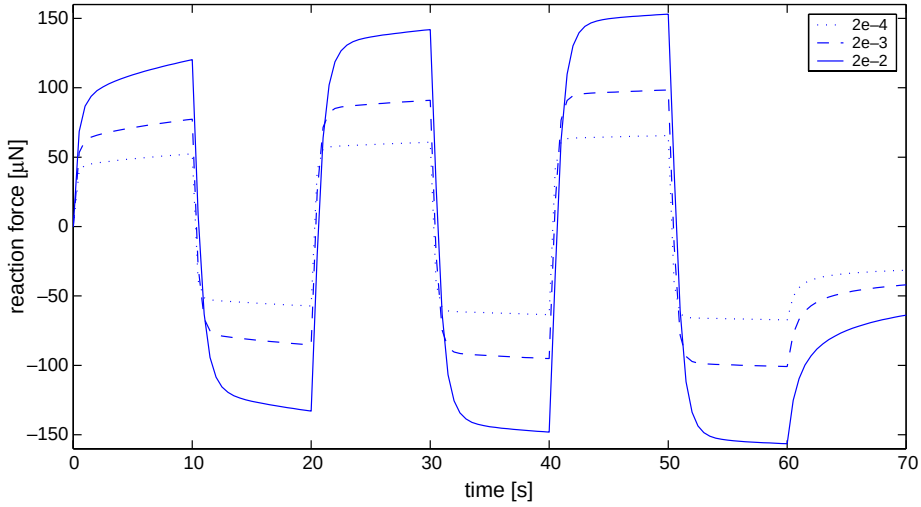

Fig. 13. Reaction force versus time for various strain rates, as-cast microstructure.

the most prominent localisation site for the two microstructures, while the difference in the sizes of the microstructures is not pronounced.

The reason behind the strengthening effect can be seen in Fig. 10. For the initial microstructure, with the smallest phase region size, the effective viscoplastic strain distributed relatively evenly over the material. This indicates that the deformation needed to accommodate the prescribed displacement occurred in both phases. However, as the microstructure coarsens more of the viscoplastic strain is confined to the softer Pb-rich phase. Fig. 10(d) shows almost no viscoplastic deformation occurred in the Sn-rich phase. This means that only the soft phase has to undergo deformation which leads to a lower required force for this case compared to a fine microstructure.

To demonstrate the influence of the strain rate the as-cast microstructure is also loaded with rates of respectively 2×10^{-4} and 2×10^{-2}. Fig. 13 shows the reaction forces versus time for the three strain rates. Increasing the rate also increases the flow stress and reaction force. The stress and effective viscoplastic strain fields show similar behaviour, see Figs. 14–16. The localisation occurs in the same positions for

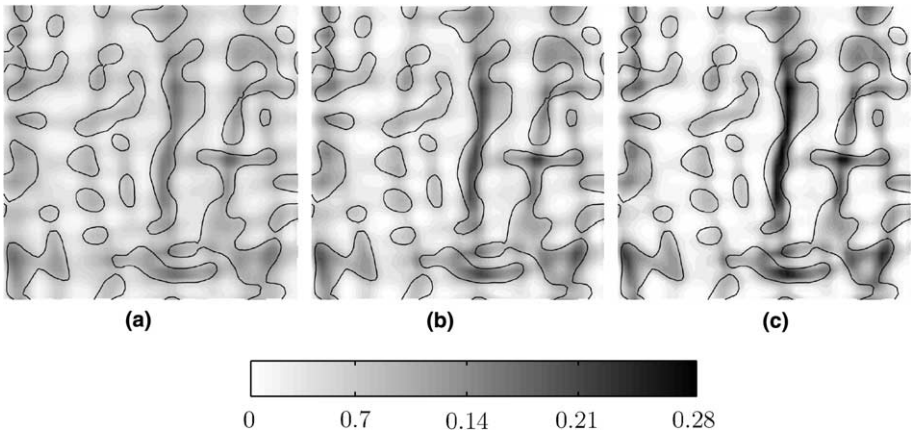

Fig. 14. Equivalent viscoplastic strain at 70 s for various strain rates, as-cast microstructure: (a) strain rate 2×10^{-4}, (b) strain rate 2×10^{-3}, (c) strain rate 2×10^{-2}.

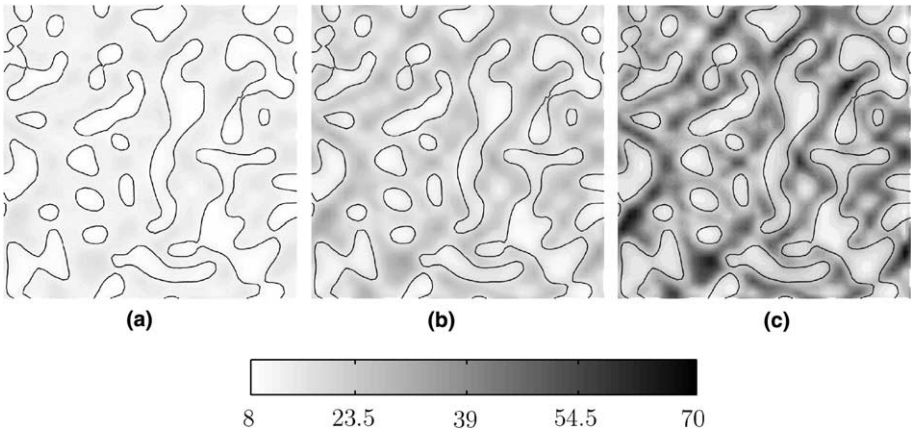

Fig. 15. Equivalent Cauchy stress in MPa at $t = 60$ for different strain rates, as-cast microstructure: (a) strain rate 2×10^{-4}, (b) strain rate 2×10^{-3}, (c) strain rate 2×10^{-2}.

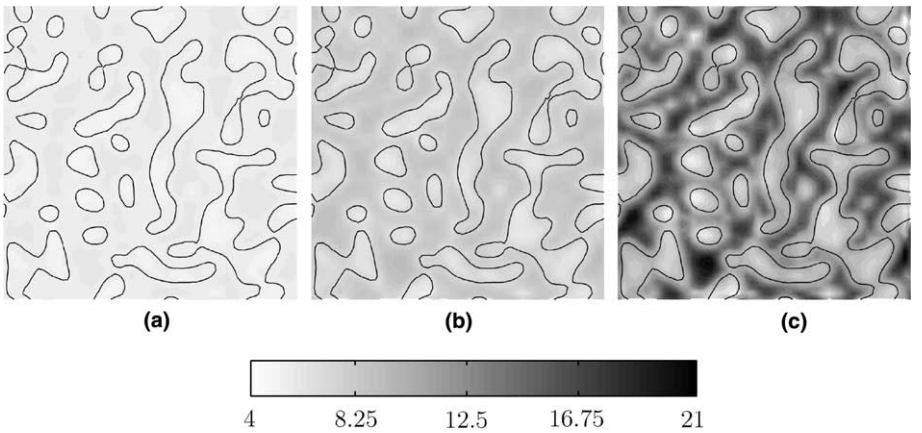

Fig. 16. Equivalent Cauchy stress in MPa at $t = 70$ for different strain rates, as-cast microstructure: (a) strain rate 2×10^{-4}, (b) strain rate 2×10^{-3}, (c) strain rate 2×10^{-2}.

all strain rates, but increases in intensity. Note that the increase of ε_{vp} with increasing strain rate also results in higher residual stresses.

7. Discussion and conclusions

A model is presented to describe the mechanical behaviour of microstructure dependent materials. The model describes the microstructure evolution using a phase field approach and employs a constitutive model dependent on the phase field to account for the underlying microstructure. It has been demonstrated by applying it to eutectic tin–lead solder, a material whose mechanical characteristics are strongly influenced by its continuously evolving microstructure. For the constitutive behaviour the elasto-viscoplastic Perzyna model has been adopted. The Perzyna model allows the use of different hardening functions, which makes it suitable for a large variety of materials. It is coupled to the phase field model through the model parameters which are taken dependent on the mass fraction field resulting from the solution of the phase field equations. In this way the microstructure is accounted for using a continuum mechanics approach. The approach does not require interface tracking methods since all information about the interface is included in the phase field. Furthermore, the evolution of a microstructure can be calculated using one mesh, no remeshing needs to be done.

Two-dimensional simulations of cyclic shearing have been performed using various microstructures. These microstructures were obtained by performing a simulation of static ageing of eutectic tin–lead at 150 °C with the phase field model. The mechanical simulations demonstrate a dependency of the material behaviour on the microstructure. Microstructures that have been aged for longer periods of time not only show larger microstructural length scales, but also a decrease in resulting reaction force, indicating microstructural softening of the material.

The difference between the various microstructures is even more pronounced when the stress field and the effective viscoplastic strain rate are examined locally. As the microstructural length scales increase, more pronounced localisation patterns are found. Both σ_{eq} and ε_{vp} locally reach significantly higher values for aged microstructures. Because of the difference between the yield stress of the two phases present in the material, most plastic flow occurs in the softer α-phase. Locally the plastic strain can reach values much higher than the macroscopically applied strain. Due to this heterogeneous plastic straining residual stresses appear in the material after relaxation.

Frear et al. (1988) found that regions of high strain in the eutectic tin–lead show a higher degree of coarsening. Furthermore, it is found that these regions of inhomogeneous coarsening are the crack nucleation sites during thermal cycling (Frear, 1989; Hacke et al., 1998). The cracks occur on the interface between the Sn-rich and the Pb-rich phase (Frear, 1989; Zhao et al., 2000). The results presented in this paper demonstrate that a coarser microstructure leads to significantly higher local values of the viscoplastic strain and of the stresses. Future work will be focussed on the incorporation of damage into the presented model.

Acknowledgments

This research is supported by the Technology Foundation STW, applied science division of NWO and the technology programme of the Ministry of Economic Affairs.

Appendix A. Finite element implementation

A.1. Elastic increment

For a fully elastic increment, i.e. $\varphi < 0$, the incremental update for the Kirchhoff stress tensor reads:

$$\boldsymbol{\tau} = \boldsymbol{F}_{\Delta} \cdot \boldsymbol{\tau}^{t} \cdot \boldsymbol{F}_{\Delta}^{\mathrm{c}} + \mathbb{H}(J) : \boldsymbol{e}_{\Delta}. \tag{A.1}$$

The variation of the stress then becomes:

$$\delta\boldsymbol{\tau} = \delta\boldsymbol{F}_{\Delta} \cdot \boldsymbol{\tau}^{t} \cdot \boldsymbol{F}_{\Delta}^{\mathrm{c}} + \boldsymbol{F}_{\Delta} \cdot \boldsymbol{\tau}^{t} \cdot \delta\boldsymbol{F}_{\Delta}^{\mathrm{c}} + \frac{\partial \mathbb{H}}{\partial J} : \boldsymbol{e}_{\Delta}\delta J + \mathbb{H}(J) : \delta\boldsymbol{e}_{\Delta}, \tag{A.2a}$$

$$\delta\boldsymbol{\tau} = \delta\boldsymbol{F}_{\Delta} \cdot \boldsymbol{F}_{\Delta}^{-1} \cdot \boldsymbol{F}_{\Delta} \cdot \boldsymbol{\tau}^{t} \cdot \boldsymbol{F}_{\Delta}^{\mathrm{c}} + \boldsymbol{F}_{\Delta} \cdot \boldsymbol{\tau}^{t} \cdot \boldsymbol{F}_{\Delta}^{\mathrm{c}} \cdot \boldsymbol{F}_{\Delta}^{-\mathrm{c}} \cdot \delta\boldsymbol{F}_{\Delta}^{\mathrm{c}} + J\frac{\partial \mathbb{H}}{\partial J} : \boldsymbol{e}_{\Delta}\boldsymbol{F}^{-1} : \delta\boldsymbol{F} - \mathbb{H}$$
$$: \frac{1}{2}\left(\delta\boldsymbol{F}_{\Delta}^{-\mathrm{c}} \cdot \boldsymbol{F}_{\Delta}^{-1} + \boldsymbol{F}_{\Delta}^{-\mathrm{c}} \cdot \delta\boldsymbol{F}_{\Delta}^{-1}\right), \tag{A.2b}$$

$$\delta\boldsymbol{\tau} = \boldsymbol{L}_{\delta} \cdot \boldsymbol{F}_{\Delta} \cdot \boldsymbol{\tau}^{t} \cdot \boldsymbol{F}_{\Delta}^{\mathrm{c}} + \boldsymbol{F}_{\Delta} \cdot \boldsymbol{\tau}^{t} \cdot \boldsymbol{F}_{\Delta}^{\mathrm{c}} \cdot \boldsymbol{L}_{\delta}^{\mathrm{c}} + \left[J\frac{\partial \mathbb{H}}{\partial J} : \boldsymbol{e}_{\Delta}\boldsymbol{I}\right] : \boldsymbol{L}_{\delta}^{\mathrm{c}} + \mathbb{H}$$
$$: \frac{1}{2}\left[\boldsymbol{F}_{\Delta}^{-\mathrm{c}} \cdot \delta\boldsymbol{F}_{\Delta}^{\mathrm{c}} \cdot \boldsymbol{F}_{\Delta}^{-\mathrm{c}} \cdot \boldsymbol{F}_{\Delta}^{-1} + \boldsymbol{F}_{\Delta}^{-\mathrm{c}} \cdot \boldsymbol{F}_{\Delta}^{-1} \cdot \delta\boldsymbol{F}_{\Delta} \cdot \boldsymbol{F}_{\Delta}^{-1}\right], \tag{A.2c}$$

$$\delta\boldsymbol{\tau} = \left[2\mathbb{I}^{S} \cdot \boldsymbol{F}_{\Delta} \cdot \boldsymbol{\tau}^{t} \cdot \boldsymbol{F}_{\Delta}^{\mathrm{c}}\right] : \boldsymbol{L}_{\delta}^{\mathrm{c}} + \left[J\frac{\partial \mathbb{H}}{\partial J} : \boldsymbol{e}_{\Delta}\boldsymbol{I}\right] : \boldsymbol{L}_{\delta}^{\mathrm{c}} + \mathbb{H} : \frac{1}{2}\left[\boldsymbol{L}_{\delta}^{\mathrm{c}} \cdot \boldsymbol{F}_{\Delta}^{-\mathrm{c}} \cdot \boldsymbol{F}_{\Delta}^{-1} + \boldsymbol{F}_{\Delta}^{-\mathrm{c}} \cdot \boldsymbol{F}_{\Delta}^{-1} \cdot \boldsymbol{L}_{\delta}\right], \tag{A.2d}$$

$$\delta\boldsymbol{\tau} = \left[2\mathbb{I}^{S} \cdot \boldsymbol{F}_{\Delta} \cdot \boldsymbol{\tau}^{t} \cdot \boldsymbol{F}_{\Delta}^{\mathrm{c}} + J\frac{\partial \mathbb{H}}{\partial J} : \boldsymbol{e}_{\Delta}\boldsymbol{I}\right] : \boldsymbol{L}_{\delta}^{\mathrm{c}} + \mathbb{H} : \left[\mathbb{I}^{S} : \boldsymbol{F}_{\Delta}^{-\mathrm{c}} \cdot \boldsymbol{F}_{\Delta}^{-1} \cdot \boldsymbol{L}_{\delta}\right], \tag{A.2e}$$

$$\delta\boldsymbol{\tau} = \mathbb{C} : \boldsymbol{L}_{\delta}^{\mathrm{c}}, \tag{A.2f}$$

with

$$\mathbb{C} = 2\mathbb{I}^{S} \cdot \boldsymbol{F}_{\Delta} \cdot \boldsymbol{\tau}^{t} \cdot \boldsymbol{F}_{\Delta}^{\mathrm{c}} + J\frac{\partial \mathbb{H}}{\partial J} : \boldsymbol{e}_{\Delta}\boldsymbol{I} + \mathbb{H} : (\mathbb{I}^{S} \cdot \boldsymbol{F}_{\Delta}^{-\mathrm{c}} \cdot \boldsymbol{F}_{\Delta}^{-1})^{\mathrm{rc}},$$

where use has been made of

$$\delta \det(\boldsymbol{A}) = \frac{\partial \det(\boldsymbol{A})}{\partial \boldsymbol{A}} : \delta \boldsymbol{A} = \det(\boldsymbol{A}) \boldsymbol{A}^{-1} : \delta \boldsymbol{A}. \tag{A.3}$$

The derivative of the material tensor $\mathbb{H}$, Eq. (46), with respect to J reads:

$$\frac{\partial \mathbb{H}}{\partial J} = -2\lambda \frac{\partial \ln(J)}{\partial J} \mathbb{I}^{\mathrm{rc}} = -2\lambda \frac{1}{J} \mathbb{I}^{\mathrm{rc}}. \tag{A.4}$$

A.2. Viscoplastic increment

The variation of the stress tensor in the case of elasto-viscoplastic behaviour, Eq. (43a), reads

$$\delta \boldsymbol{\tau} = \delta^{*}\tau - \delta \mathbb{H} : \Delta\gamma_{\mathrm{vp}} \boldsymbol{N} - \mathbb{H} : \delta\Delta\gamma_{\mathrm{vp}} \boldsymbol{N} - \mathbb{H} : \Delta\gamma_{\mathrm{vp}} \delta \boldsymbol{N}, \tag{A.5}$$

where $\delta^{*}\tau$ is the variation of the Kirchhoff stress tensor in case of purely elastic deformation. Variation of the material tensor $\mathbb{H}$, Eq. (46), the viscoplastic multiplier $\Delta\gamma_{\mathrm{vp}}$, Eq. (43b), and the plastic flow direction $\boldsymbol{N}$ respectively read

$$\delta \mathbb{H} : \Delta\gamma_{\mathrm{vp}} \boldsymbol{N} = -2K \frac{1}{J} J \boldsymbol{I} : \boldsymbol{L}^{\mathrm{c}}_{\delta} \mathbb{I}^{\mathrm{rc}} : \Delta\gamma_{\mathrm{vp}} \boldsymbol{N} = -2K \Delta\gamma_{\mathrm{vp}} \boldsymbol{N} \boldsymbol{I} : \boldsymbol{L}^{\mathrm{c}}_{\delta}, \tag{A.6}$$

$$\begin{aligned} \delta\Delta\gamma_{\mathrm{vp}} &= \Delta t \eta \delta \left(\frac{\tau_{\mathrm{eq}} - \tau_{\mathrm{y}}}{\varphi_0} \right)^{N} = N \Delta t \frac{\eta}{\tau_{\mathrm{y0}}} \left(\frac{\tau_{\mathrm{eq}} - \tau_{\mathrm{y}}}{\tau_{\mathrm{y0}}} \right)^{N-1} \left(\delta\tau_{\mathrm{eq}} - \delta\tau_{\mathrm{y}} \right) = c_1 \left(\boldsymbol{N} : \delta\boldsymbol{\tau} - \frac{\partial \tau_{\mathrm{y}}}{\partial \Delta\gamma_{\mathrm{vp}}} \delta\Delta\gamma_{\mathrm{vp}} \right) \\ &= c_2 \boldsymbol{N} : \delta\boldsymbol{\tau}, \end{aligned} \tag{A.7}$$

with

$$c_1 = N \Delta t \frac{\eta}{\varphi_0} \left(\frac{\tau_{\mathrm{eq}} - \tau_{\mathrm{y}}}{\varphi_0} \right)^{N-1} \quad \text{and} \quad c_2 = \frac{c_1}{1 + \frac{\partial \tau_{\mathrm{y}}}{\partial \varepsilon_{\mathrm{vp}}} \frac{\partial \varepsilon_{\mathrm{vp}}}{\partial \Delta\gamma_{\mathrm{vp}}} c_1}, \tag{A.8}$$

and

$$\delta \boldsymbol{N} = \frac{3}{2} \frac{1}{\tau_{\mathrm{eq}}} \delta\boldsymbol{\tau}^{\mathrm{d}} - \frac{3}{2} \frac{\tau^{\mathrm{d}}}{\tau^{2}_{\mathrm{eq}}} \delta\tau_{\mathrm{eq}} = \frac{3}{2} \frac{1}{\tau_{\mathrm{eq}}} \left(\delta\boldsymbol{\tau} - \frac{1}{3} \boldsymbol{I}\boldsymbol{I} : \delta\boldsymbol{\tau} \right) - \frac{1}{\tau_{\mathrm{eq}}} \boldsymbol{N}\boldsymbol{N} : \delta\boldsymbol{\tau} = \frac{1}{\tau_{\mathrm{eq}}} \left(\frac{3}{2} \mathbb{I} - \frac{1}{2} \boldsymbol{I}\boldsymbol{I} - \boldsymbol{N}\boldsymbol{N} \right) : \delta\boldsymbol{\tau}. \tag{A.9}$$

Substituting Eqs. (A.6), (A.7), and (A.9) in Eq. (A.5) then results in

$$\delta \boldsymbol{\tau} = \mathbb{N}^{-1} : (\mathbb{C} + \mathbb{T}) : \boldsymbol{L}^{\mathrm{c}}_{\delta}, \tag{A.10}$$

with

$$\mathbb{T} = 2\Delta\gamma_{\mathrm{vp}} \lambda \boldsymbol{N}\boldsymbol{I}, \tag{A.11}$$

and

$$\mathbb{N} = \mathbb{I} + c_2 \mathbb{H} : \boldsymbol{N}\boldsymbol{N} + \mathbb{H} : \Delta\gamma_{\mathrm{vp}} \frac{1}{\tau_{\mathrm{eq}}} \left(\frac{3}{2} \mathbb{I} - \frac{1}{2} \boldsymbol{I}\boldsymbol{I} - \boldsymbol{N}\boldsymbol{N} \right). \tag{A.12}$$

A.3. Stress update algorithm

It can be shown that for the current hyperelastic model the direction of plastic flow is fully determined by the elastic predictor state, $\boldsymbol{N} = {}^{*}\boldsymbol{N}$.

$$\boldsymbol{\tau} = {}^{*}\boldsymbol{\tau} - 3[\mu - \lambda \ln(J)]\mathbb{I}^{\mathrm{rc}} : \Delta\gamma_{\mathrm{vp}} \frac{\boldsymbol{\tau}^{\mathrm{d}}}{\tau_{\mathrm{eq}}}, \tag{A.13a}$$

$$\boldsymbol{\tau}^{\mathrm{d}} = {}^{*}\boldsymbol{\tau}^{\mathrm{d}} - 3[\mu - \lambda \ln(J)]\mathbb{I}^{\mathrm{rc}} : \Delta\gamma_{\mathrm{vp}} \frac{\boldsymbol{\tau}^{\mathrm{d}}}{\tau_{\mathrm{eq}}}, \tag{A.13b}$$

$$\boldsymbol{\tau}^{\mathrm{d}} = {}^{*}\boldsymbol{\tau}^{\mathrm{d}} - 3[\mu - \lambda \ln(J)] \frac{\Delta\gamma_{\mathrm{vp}}}{\tau_{\mathrm{eq}}} \boldsymbol{\tau}^{\mathrm{d}}, \tag{A.13c}$$

$$\boldsymbol{\tau}^{\mathrm{d}} = \left\{ 1 + 3[\mu - \lambda \ln(J)] \frac{\Delta\gamma_{\mathrm{vp}}}{\tau_{\mathrm{eq}}} \right\}^{-1} {}^{*}\boldsymbol{\tau}^{\mathrm{d}}, \tag{A.13d}$$

$$\tau_{\mathrm{eq}} = \left\{ 1 + 3[\mu - \lambda \ln(J)] \frac{\Delta\gamma_{\mathrm{vp}}}{\tau_{\mathrm{eq}}} \right\}^{-1} {}^{*}\tau_{\mathrm{eq}}. \tag{A.13e}$$

Furthermore, for the stress update algorithm the nodal displacements are known and fixed, except for the plane stress case. Therefore the volume and the stresses of the elastic predictor will not change, i.e. δJ and $\delta {}^{*}\tau$ are zero.

To use the Newton–Raphson method system (43) is first rewritten into

$$\boldsymbol{\tau} - {}^{*}\boldsymbol{\tau} + \mathbb{H} : \boldsymbol{N}\Delta\gamma_{\mathrm{vp}} = 0, \tag{A.14a}$$

$$\Delta\gamma_{\mathrm{vp}} - \Delta t \eta \left(\frac{\varphi}{\varphi_0} \right)^{N} = 0. \tag{A.14b}$$

Decomposing system (43) in an iterative manner thus results in

$$\boldsymbol{\tau} + \delta\boldsymbol{\tau} - {}^{*}\boldsymbol{\tau} + \mathbb{H} : \boldsymbol{N}(\Delta\gamma_{\mathrm{vp}} + \delta\Delta\gamma_{\mathrm{vp}}) = 0, \tag{A.15a}$$

$$\Delta\gamma_{\mathrm{vp}} + \delta\Delta\gamma_{\mathrm{vp}} - \Delta t \eta \left(\frac{\varphi}{\varphi_0} \right)^{N} - \frac{\Delta t \eta N}{\varphi_0} \left(\frac{\varphi}{\varphi_0} \right)^{N-1} \delta\varphi = 0. \tag{A.15b}$$

Substituting the definition of the yield function $\varphi = \tau_{\mathrm{eq}} - \tau_{\mathrm{y}}$ and using the variation of τ_{eq},

$$\delta\tau_{\mathrm{eq}} = \frac{1}{2} \left(\frac{3}{2} \boldsymbol{\tau}^{\mathrm{d}} : \boldsymbol{\tau}^{\mathrm{d}} \right)^{-1/2} 2 \left(\frac{3}{2} \boldsymbol{\tau}^{\mathrm{d}} : \delta\boldsymbol{\tau}^{\mathrm{d}} \right) \tag{A.16}$$

$$= \frac{3}{2} \frac{1}{\tau_{\mathrm{eq}}} \boldsymbol{\tau}^{\mathrm{d}} : \delta\boldsymbol{\tau} - \boldsymbol{\tau}^{\mathrm{d}} : \frac{1}{3} \boldsymbol{II} : \delta\boldsymbol{\tau} \tag{A.17}$$

$$= \frac{3}{2} \frac{1}{\tau_{\mathrm{eq}}} \left(\boldsymbol{\tau}^{\mathrm{d}} - \boldsymbol{\tau}^{\mathrm{d}} : \frac{1}{3} \boldsymbol{II} \right) : \delta\boldsymbol{\tau} \tag{A.18}$$

$$= \frac{3}{2} \frac{\tau^{\mathrm{d}}}{\tau_{\mathrm{eq}}} : \delta\boldsymbol{\tau} = \boldsymbol{N} : \delta\boldsymbol{\tau}, \tag{A.19}$$

then results in

$$\mathbb{I} : \delta\boldsymbol{\tau} + \mathbb{H} : \boldsymbol{N}\delta\Delta\gamma_{\mathrm{vp}} = {}^{*}\boldsymbol{\tau} - \boldsymbol{\tau} - \mathbb{H} : \boldsymbol{N}\Delta\gamma_{\mathrm{vp}}, \tag{A.20a}$$

$$\delta\Delta\gamma_{\mathrm{vp}} - c_1(\boldsymbol{N} : \delta\boldsymbol{\tau} - \delta\tau_{\mathrm{y}}) = \Delta t\eta\left(\frac{\varphi}{\varphi_0}\right)^{N} - \Delta\gamma_{\mathrm{vp}}, \tag{A.20b}$$

with

$$c_1 = \frac{\Delta t\eta N}{\varphi_0}\left(\frac{\varphi}{\varphi_0}\right)^{N-1}. \tag{A.21}$$

Assuming the incremental hardening law to be a function of $\Delta\gamma_{\mathrm{vp}}$ only, i.e. the yield stress can be a function of the viscoplastic multiplier and/or its rate the system that needs to be solved then becomes

$$\mathbb{I} : \delta\boldsymbol{\tau} + \mathbb{H} : \boldsymbol{N}\delta\Delta\gamma_{\mathrm{vp}} = {}^{*}\boldsymbol{\tau} - \boldsymbol{\tau} - \mathbb{H} : \boldsymbol{N}\Delta\gamma_{\mathrm{vp}}, \tag{A.22a}$$

$$-c_1\boldsymbol{N} : \delta\boldsymbol{\tau} + \left(1 + c_1\frac{\partial\tau_{\mathrm{y}}}{\partial\Delta\gamma_{\mathrm{vp}}}\right)\delta\Delta\gamma_{\mathrm{vp}} = \Delta t\eta\left(\frac{\varphi}{\varphi_0}\right)^{N} - \Delta\gamma_{\mathrm{vp}}. \tag{A.22b}$$

References

Amagai, M., 1999. Chip scale package (csp) solder joint reliability and modeling. Microelectronics Reliability 39 (4), 463–477.

Anand, L., 1985. Constitutive relations for hot working of metals. Journal of Plasticity 1, 213–231.

Artemev, A., Wang, Y., Khachaturyan, G., 2000. Three-dimensional phase field model and simulation of martensitic transformation in multilayer systems under applied stresses. Acta Materialia 48, 2503–2518.

Basaran, C., Chanderoy, R., 1998. Mechanics of Pb40/Sn60 near-eutectic solder alloys subjected to vibration. Applied Mathematical Modelling 22, 601–627.

Basaran, C., Chanderoy, R., 2000. Using finite element analysis for simulation of reliability tests on solder joints in microelectronic packaging. Computers and Structures 74, 215–231.

Basaran, C., Tang, H., 2002. Implementation of a thermodynamic framework for damage mechanics of solder interconnects in microelectronic packaging. International Journal of Damage Mechanics 11.

Basaran, C., Desai, C., Kundu, T., 1998. Thermomechanical finite element analysis of problems in electronic packaging using the disturbed state concept. Part I: Theory and formulation. Journal of Electronic Packaging 120 (1), 41–47.

Brandon, D., 1994. Nonlocal superconductivity. Zeitschrift für angewandte Mathematik und Mechanik 45, 135–152.

Cahn, J., Hilliard, J., 1958. Free energy of a nonuniform system, I: Interfacial energy. The Journal of Chemical Physics 28 (2), 258–267.

Cheng, Z., Wang, G., Chen, L., Wilde, J., Becker, K., 2000. Viscoplastic Anand model for solder alloys and its application. Soldering and Surface Mount Technology 12 (2), 31–36.

Clark, M., Aldan, T., 1973. Deformation enhanced grain growth in a superplastic Sn–1%Bi alloy. Acta Metallurgica 21, 1195–1206.

Darveaux, R., Banerji, K., 1992. Constitutive relations for tin-based solder joints. IEEE Transactions on Components, Hybrids, and Manufacturing Technology 15 (6), 1013–1024.

Dreyer, W., Müller, W., 2000. A study of the coarsening in tin/lead solders. International Journal of Solids and Structures 37, 3841–3871.

Dreyer, W., Müller, W., 2001. Modelling diffusional coarsening in eutectic tin/lead solders: a quantitative approach. International Journal of Solids and Structures 38, 1433–1458.

Evers, L., Brekelmans, W., Geers, M., 2004. Scale dependent crystal plasticity framework with dislocation density and grain boundary effects. International Journal of Solids and Structures 41, 5209–5330.

Fosdick, R., Mason, D., 1998. On a model of nonlocal continuum mechanics, Part I: Existence and regularity. SIAM Journal of Applied Mathematics 58 (4), 1278–1306.

Frear, D., 1989. Thermomechanical fatigue of solder joints: a new comprehensive test method. IEEE Transactions on Composites, Hybrids, and Manufacturing Technology 12 (4), 492–501.

Frear, D., Grivas, D., Morris Jr., J., 1988. A microstructural study of the thermal fatigue failures of 60Sn–40Pb solder joints. Journal of Electronic Materials 17, 171–180.

Frear, D., Burchet, S., Neilsen, M., Stephens, J., 1997. Microstructurally based finite element simulation on solder joint behaviour. Soldering and Surface Mount Technology 9 (1), 39–42.

Gajewski, H., Zacharias, K., 2003. On a nonlocal phase separation model. Journal of Mathematical Analysis and Applications 286, 11–31.

Giacomin, G., Lebowitz, J., 1997. Phase segregation dynamics in particle systems with long range interactions. I. Macroscopic limits. Journal of Statistical Physics 87 (1), 37–61.

Hacke, P., Sprecher, A., Conrad, H., 1998. Microstructure coarsening during thermo-mechanical fatigue of Pb–Sn solder joints. Journal of Electronic Materials 26 (7), 774–782.

Ju, S., Kuskowski, S., Sandor, B., Plesha, M., 1994. Creep-fatigue damage analysis of solder joints. In: Schroeder, S., Mitchell, M. (Eds.), Fatigue of Electronic Materials, STP-1153. American Society for Testing and Materials, Philadelphia, pp. 1–21.

Kouznetsova, V., Brekelmans, W., Baaijens, F., 2001. An approach to micro–macro-modeling of heterogeneous materials. Computational Mechanics 27, 37–48.

Leo, P., Lowengrub, J., Jou, H., 1998. A diffuse interface model for microstructural evolution in elastically stressed solids. Acta Metallurgica 46 (6), 2113–2130.

Lifshitz, I., Slyozov, V., 1961. The kinetics of precipitation from supersaturated solid solutions. The Journal of Physics and Chemistry of Solids 19, 35–50.

Matin, M., Vellinga, W., Geers, M.., 2004. Aspects of coarsening in eutectic Sn–Pb. Acta Materialia 52, 3475–3482.

Ni, Y., He, L., Yin, L., 2002. Three-dimensional phase field modeling of phase separation in strained alloys. Materials Chemistry and Physics 78, 442–447.

Peerlings, R., Geers, M., de Borst, R., Brekelmans, W., 2001. A critical comparison of nonlocal and gradient-enhanced continua. International Journal of Solids and Structures 38, 7723–7746.

Perić, D., 1992. On consistent stress rates in solid mechanics: computational implications. International Journal for Numerical Methods in Engineering 33, 799–817.

Perić, D., 1993. On a class of constitutive equations in viscoplasticity: formulation and computational issues. International Journal for Numerical Methods in Engineering 36, 1365–1393.

Perzyna, P., 1966. Fundamental problems in visco-plasticity. Recent Advances in Applied Mechanics. Academic Press, New York.

Perzyna, P., 1971. Thermodynamic theory of viscoplasticityAdvances in Applied Mechanics, vol. 11. Academic Press, New York, pp. 313–354.

Perzyna, P., 1985. On constitutive modelling of dissipative solids for plastic flow, instability and fracture. In: Sawczuk, A., Bianchi, G. (Eds.), Plasticity Today: Modelling, Methods and Applications. Elsevier Applied Science Publishers, pp. 657–679.

Senkov, O., Myshlyaev, M., 1986. Grain growth in a superplastic Zn–22%Al alloy. Acta Metallurgica 34, 97–106.

Sluis, O.v.d., Schreurs, P., Meijer, H., 1999. Effective properties of a viscoplastic constitutive model obtained by homogenisation. Mechanics of Materials 31, 743–759.

Smit, R., Brekelmans, W., Meijer, H., 1999. Prediction of the large-strain mechanical response of heterogeneous polymer systems: local and global deformation behaviour of a representative volume element of voided polycarbonate. Journal of the Mechanics and Physics of Solids 47, 201–221.

Ubachs, R., Schreurs, P., Geers, M., 2003. Microstructure evolution of tin–lead solder. EuroSIME 2003, Aix-en-Provence, France.

Ubachs, R., Schreurs, P., Geers, M., 2004. A nonlocal diffuse interface model for microstructure evolution of tin–lead solder. Journal of the Mechanics and Physics of Solids 52 (8), 1763–1792.

Vianco, P., Burchet, S., Neilsen, M., Rejent, J., Frear, D., 1999. Coarsening of the Sn–Pb solder microstructure in constitutive model-based predictions of solder joint thermal mechanical fatigue. Journal of Electronic Materials 28 (11), 1290–1298.

Wang, G., Chen, Z., Becker, K., Wilde, J., 2001. Applying Anand model to represent the viscoplastic behaviour of solder alloys. Journal of Electronic Packaging 123, 247–253.

Zhao, Y., Miyashita, C., Mutoh, Y., 2000. Fatigue crack growth behavior of 95Pb–5Sn solder under various stress ratios and frequencies. International Journal of Fatigue 22, 665–673.

Zhu, J., Chen, L.-Q., Shen, J., Tikare, V., 1999. Coarsening kinetics from a variable-mobility Cahn–Hilliard equation: application of a semi-implicit Fourier spectral method. Physical Review E 60 (4), 3564–3572.

Zhu, J., Chen, L.-Q., Shen, J., 2001. Morphological evolution during phase separation and coarsening with strong inhomogeneous elasticity. Modelling and Simulation in Materials Science and Engineering 9, 499–511.